Fall 2010

Numerical Simulation of Capsule Dissolution in the USP Apparatus II

Jasmine Han
San Jose State University

NUMERICAL SIMULATION OF CAPSULE DISSOLUTION IN THE USP APPARATUS II

A Thesis

Presented to

The Faculty of the Department of Chemical and Materials Engineering

San José State University

In Partial Fulfillment

of the Requirements for the Degree

Master of Science

by

Jasmine E. Han

December 2010

The Designated Thesis Committee Approves the Thesis Titled

NUMERICAL SIMULATION OF CAPSULE DISSOLUTION IN THE USP APPARATUS II

by

Jasmine E. Han

APPROVED FOR THE DEPARTMENT OF CHEMICAL AND

MATERIALS ENGINEERING

December 2010

Dr. Gregory Young	Department of Chemical and Materials Engineering
Dr. Melanie McNeil	Department of Chemical and Materials Engineering
Dr. Otute Akiti	Exelixis Inc.

ABSTRACT

NUMERICAL SIMULATION OF CAPSULE DISSOLUTION IN THE USP APPARATUS II

by Jasmine E. Han

The capsule is the second most common type of drug dosage form, yet detailed research of capsule dissolution in the USP Apparatus II (a paddle dissolution apparatus that mimics the drug dissolution process in an *in vivo* environment) is not well reported. In this work, a mathematical model was developed that incorporates both the dissolution of the capsule shell and the slug within the capsule shell. Capsule shell dissolution was modeled with the assumption that the shell undergoes an erosion process only. The capsule slug dissolution model incorporated mass transfer principles, Markov chain theory, and the influence of hydrodynamics on capsules dissolution using computational fluid dynamics (CFD)-predicted velocity profiles. To complete the model, the mass transfer coefficients (determined experimentally and theoretically) were incorporated. The model was validated by statistically comparing the simulated profiles to the experimental data using the similarity factor. In addition, this model can provide insights into the dissolution mechanism where a drug product may either disintegrate or erode during dissolution testing. This capsule slug dissolution model has the potential to reduce substantially the number of time-consuming physical dissolution experiments and maximize the efficiency of process development.

ACKNOWLEDGEMENTS

I would like to thank my advisor Dr. Gregory Young for providing countless support and valuable advice throughout my master's program at San José State University. I really appreciate his willingness to accommodate the schedule of a part-time student with a full-time job by meeting with me early in the morning before I go to work. I would also like to thank Dr. Melanie McNeil for her extensive comments and numerous reminders to polish this paper. My deepest appreciation goes to Dr. Otute Akiti who has given me the opportunity to work on this research project. I sincerely thank him for his tremendous help, support, and sharing his exceptional knowledge in this work. Being a wonderful and a patient advisor, he definitely has made my thesis research a very enjoyable process. I will be forever in-debt for everything that he has done for me.

I would like to thank the staff members of South Bay Church and the Trio small group members of Crosspoint Church of Silicon Valley for their innumerable prayers, help, and support. Last but not least, I would like to offer my sincere gratitude to Dr. Otute Akiti, Dr. Sarina Ma, Ms. Crystal Pollock-Dove, and Ms. Andrea Smith for their support and help in editing this paper.

Table of Contents

List of Figures

List of Tables

List of Symbols Used

A	surface area of solid dosage (mm^2)
$A(C)$	surface area as a function of concentration C (mm^2)
$A(t)$	surface area as a function of time t (mm^2)
A_G	initial surface area of capsule shell (mm^2)
$A_{Sl,b}$	surface area of unbroken slug at time t_b (mm^2)
$A_{Sl,b+1}$	surface area of unbroken slug at time t_{b+1} (mm^2)
A_{top}	surface area of the top of tablet (mm^2)
A_{side}	surface area of the side of tablet (mm^2)
A_{Sl}	slug surface area (mm^2)
A_{si}	surface area of individual disintegrated particles (mm^2)
$A_{Tpi}(t_b)$	surface area of all the disintegrated particles at each state x_i at time t_b (mm^2)
$A(t_b)$	overall surface area from all the disintegrated particles and unbroken slug (mm^2)
$\boldsymbol{a}(t)$	state probability vector at time t (dimensionless)
$\boldsymbol{a}(t+\tau)$	state probability vector at time $t+\tau$ (dimensionless)
a_i	state probability of particle size of state x_i on each sieve fraction (dimensionless)
$a_i(t_0)$	state probability of particle size of state x_i at time t_0 (dimensionless)
$a_i(t_b)$	state probability of particle size of state x_i at time t_b (dimensionless)
$\boldsymbol{B}$	probability distribution matrix (dimensionless)
B_i	row i of matrix **B** (dimensionless)
$b(x,y)$	probability distribution for size x particles formed from size y particles
b_{ji}	probability distribution for particles in state I formed from breakage of particles in state j
C	drug concentration (mg/mL)
C_0	initial drug concentration (mg/mL)
C_s	saturated drug solubility (mg/mL)
C_t	drug concentration at time t (mg/mL)
$C(t)$	drug concentration as a function of time t (mg/mL)
$C(t_b)$	drug concentration at time t_b (mg/mL)
$C_T(t)$	overall shell plus slug concentration as a function of time t (mg/mL)
$\boldsymbol{D}$	diagonal matrix (dimensionless)
D_{ii}	diagonal value of matrix **D** (dimensionless)
D_{AB}	diffusion coefficient or diffusivity (m^2/s)
d	agitator/impeller diameter (cm)
d_{i-1}	lower limit of state interval i (mm)
d_i	upper limit of state interval i (mm)
d_{j-1}	lower limit of state interval j (mm)
d_{Sl}	slug diameter (mm)
d_{Sl0}	initial slug diameter (mm)
d_T	diameter of tablet (mm)
f_1	difference factor (dimensionless)
f_2	similarity factor (dimensionless)
$f(x,t)$	number density function for size x particles at time t

$f(y,t)$	number density function for size y particles at time t
G	solubility of gelatin shell (mg/ml)
G_s	saturated solubility of gelatin (mg/ml)
$G(t)$	gelatin concentration as a function of time t (mg/mL)
$\boldsymbol{g}$	gravitational acceleration vector (m/s^2)
h	diffusion layer thickness (mm)
i	state number (dimensionless)
k	mass transfer coefficient (m/s)
k_G	mass transfer coefficient of gelatin shell (m/s)
k_{exp}	experimental mass transfer coefficient (m/s)
k_{theo}	theoretical mass transfer coefficient (m/s)
k_N	constant in Noyes-Whitney equation (s^{-1})
k_{top}	mass transfer coefficient on the top of tablet (m/s)
k_{side}	mass transfer coefficient on the side of tablet (m/s)
$\boldsymbol{L}$	lower triangular matrix (dimensionless)
L_i	row i of matrix **L** (dimensionless)
L_{Sl}	length of slug (mm)
L_{Sl0}	initial length of slug (mm)
M	molecular weight (kg/kmol)
m	mass of drug diffused into fluid (mg)
N	rotational speed of the agitator/impeller (rotations/s)
$N_i(t)$	number of particles in state i at time t
$N_j(t)$	number of particles in state j at time t
$\Delta N_i(t)$	rate of change of number of particles
n	number of time points (dimensionless)
$n_i(t_b)$	number of particles in each state x_i at time t_b (dimensionless)
$\boldsymbol{P}$	Markovian transition matrix (dimensionless)
p	fluid pressure ($kg/m \cdot s^2$)
p_{ij}	probability of transition from state i to state j (dimensionless)
R	ratio of r to r_w (dimensionless)
R_t	dissolution value of the reference assay at time t (%)
Re	Reynolds number (dimensionless)
Re_Ω	rotating Reynolds number (dimensionless)
r	distance in radial direction (mm)
$r_{Sl,0}$	initial slug radius (mm)
$r_{Sl,b+1}$	radius of the unbroken slug at time t_{b+1} (mm)
$r_{nSl,b}$	radius of the slug after diffusion at time t_b (mm)
r_w	radius of the cylindrical part of the vessel (mm)
$S(x)$	breakage frequency of size x particles
$S(y)$	breakage frequency of size y particles
Sc	Schmidt number (dimensionless)
S_i	breakage frequency of particles in state i
S_j	breakage frequency of particles in state j
T	vessel diameter (cm)

T_K temperature of the system (K)
T_t dissolution value of the test assay at time t (%)
t time (minute)
t_b time at time step b (minute)
t_{b+1} time at time step b+1 (minute)
t_G time for capsule shell dissolution (minute)
u_Ω velocity at the periphery of the cylinder (mm/min)
V_A molar volume of the solute at its normal boiling point (m^3/kmol)
$V_{dif,b}$ volume of the sample dissolved at time t_b (mm^3)
$V_i(t_b)$ total volume of disintegrated particles at each particle size of state x_i (mm^3)
V_L dissolution medium volume (mL)
$V_{p,b}$ total volume of freshly disintegrated particles from the slug at time t_b (mm^3)
$V_{p,b+1}$ total volume of freshly disintegrated particles from the slug at time t_{b+1} (mm^3)
$V_{Lp,b}$ volume of leftover particles that did not dissolve at t_b (mm^3)
$V_{Lp,b+1}$ volume of leftover particles that did not dissolve at t_{b+1} (mm^3)
$V_{net,b}$ volume of total undissolved sample at time t_b (mm^3)
$V_{nSl,b}$ undissolved slug volume after dissolution at time t_b (mm^3)
$V_{np,b}$ volume of undissolved particles at time t_b (mm^3)
V_{si} volume of individual disintegrated particles (mm^3)
V_{Sl} slug volume (mm^3)
$V_{Sl,b}$ slug volume at time t_b (mm^3)
V_{Sl0} initial slug volume (mm^3)
$V_{Sl,b+1}$ volume of unbroken slug at time t_{b+1} (mm^3)
$\boldsymbol{v}$ velocity vector (m/s)
v_{tip} impeller tip speed (m/s)
v_r radial component of velocity (m/s)
v_θ tangential component of velocity (m/s)
v_z axial component of velocity (m/s)
x diameter of size x particle (μm)
x_i diameter of disintegrated particle at state i (μm)
x_{i+1} diameter of disintegrated particle at state i+1 (μm)
y diameter of size y particle (μm)
z distance from the intersection between cylindrical and hemispherical sections (mm)

Greek symbols
α particle breakage coefficient ($\mu m^{-3} \cdot s^{-1}$)
β height-to-diameter of slug (dimensionless)
γ disintegration constant (mg/mm^4)
ρ fluid density (kg/m^3)
ρ_{Sl} slug density (mg/mm^3)
μ dynamic viscosity of fluid (kg/m·s)
ν kinematic viscosity of fluid (cm^2/s)
τ time step (s)

ψ_B	association parameter (dimensionless)
ω	angular velocity (s^{-1})

CHAPTER ONE

INTRODUCTION

Oral drug delivery is the preferred route to deliver a pharmaceutical drug product to the body due to its relative ease of consumption and minimal interference with daily activities. It is preferred also because it is a pain-free process for most patients. Two of the most common oral dosage forms are tablets and capsules, while other oral drug products are packaged in sachets or solution forms. Regardless of the oral dosage form, the drug product consists of an active pharmaceutical ingredient (API) and excipient materials. The excipient materials are included in the drug product to serve as binders, disintegrants, lubricants, and dissolution enhancers.

Upon oral administration of the drug product, drug absorption and its subsequent bioavailability depend greatly on the solubility and permeability of the API and dosage form. To help predict the *in vivo* performance of a drug product, an *in vitro* dissolution test is often performed to determine the release and the dissolution profile of the drug substance. A drug dissolution test is also used to "(1) assess the lot-to-lot quality of a drug product, (2) guide development of new formulations, and (3) ensure continuing product quality and performance after certain changes" [1]. These key testing attributes reflect the extensive use of the dissolution test, its importance in the pharmaceutical industry, and its continuing role in future drug development and manufacturing processes. A model to predict the drug dissolution profile would be a valuable tool in the pharmaceutical drug development process.

1.1 The Dissolution Apparatus and the Dissolution Test Method

The dissolution apparatus is an instrument that mimics the drug dissolution process in an *in vivo* environment. A schematic diagram of a paddle dissolution apparatus is presented in Figure 1. The dissolution apparatus produces flow using an assembly that consists of a cylindrical vessel with a hemispherical bottom and a motor with a drive shaft and stirrer known as the stirring element. The liquid volume (usually 900 mL), the operating temperature (37°C), and the composition of the medium in the cylindrical vessel are selected to represent physiological conditions and allow adequate sink conditions during dissolution testing. Under sink conditions, the final drug concentration during the test is at a low enough concentration that dissolution is not hindered by solubility limits. The sink condition is usually equal to 3-10 times the solubility of the drug in the selected solution. Some common dissolution media used are water, 0.1N HCl, simulated intestinal fluid, and simulated gastric fluid.

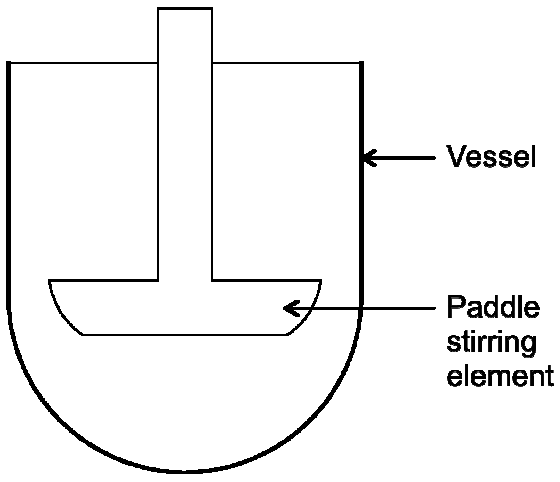

Figure 1. Schematic diagram of a dissolution apparatus.

Upon the addition of a tablet or a capsule into the dissolution vessel with the selected dissolution medium, the stirring element serves to produce consistent hydrodynamics from vessel to vessel. It also allows homogeneous drug distribution in the vessel as the drug product dissolves via the diffusion process. Even though the temperature, pH, volume of the dissolution medium, and paddle rotation speed are selected to be similar to those in the *in vivo* environment, dissolution testing has yet to completely represent the continuous change of pH, agitation rate and force, and the variable amount of fluid present along the gastrointestinal tract. Therefore, this *in vitro* dissolution experiment should not entirely replace the more expensive *in vivo* studies.

Dissolution apparatus and recommended dissolution methods are well documented in both the United States Pharmacopeia (USP) and the United States Department of Health and Human Services Food and Drug Administration (FDA) database. There are currently four dissolution test apparatus listed on the USP, namely Apparatus I (basket apparatus), Apparatus II (paddle apparatus), Apparatus III (reciprocating cylinder), and Apparatus IV (flow-through cell). Among them, the most widely adopted apparatus for tablet and capsule dissolution testing are the USP Apparatus I and the USP Apparatus II [2]. The main difference between the two is the stirring element. In Apparatus I, flow is produced by a cylindrical basket, whereas, in Apparatus II, flow is produced by a "paddle formed from a blade and a shaft" [2]. The specifications of the basket and paddle stirring elements, mandated by the USP to ensure consistency in testing, can be found in USP Chapter 711 [2]. Should a dosage form (such as a capsule) float in the dissolution medium, a sinker device is attached to the tested

drug product to force the sample to sink to the bottom of the paddle apparatus. Capsule dissolution using a paddle apparatus, one of the most common *in vitro* dissolution test apparatus to predict solid drug product performance in the *in vivo* environment, is the system of interest in this study.

In addition to the USP specifications, the FDA also heavily regulates dissolution testing requirements. To help ensure that dissolution test methods provide reliable information, the FDA's Center for Drug Evaluation and Research (CDER) provides a list of guidance documents for the industry. Furthermore, the FDA also provides recommended dissolution test methods, which include the type of apparatus, speed of the stirring element, composition and volume of the medium, and sampling times for all the drugs listed in their database [3].

1.2 Failures of Dissolution Testing

Dissolution testing is a critical test in the drug development process. It is a regulatory requirement mandated by the FDA, and the USP has provided strict dissolution apparatus specifications. The USP Apparatus II became an official test apparatus in 1978. However, the hydrodynamics within the dissolution apparatus have not been fully understood, and many inconsistent measurements and test failures have been reported [4-7]. Variability in dissolution profiles was found even with calibrator tablets [5, 8-9]. This suggests that some recalled drug products were a result of faulty apparatus configuration. In a technical report submitted to the FDA, Armenante *et al.* [10] reported that "failed dissolution tests resulted in 47 product recalls in 2000-2002, representing 16% of non-manufacturing recalls for oral solid dosage forms." Moreover,

twenty products were found on the Health Canada recall list in 2009 to 2010 [11-12]. Drug product recalls due to dissolution test failures are inevitable if the root cause is not resolved. It is vital to determine whether the failures are due to the apparatus configuration or to the drug itself.

Failures of dissolution testing can be a financial burden to pharmaceutical companies, as they increase investigation and manufacturing costs. In addition, misleading dissolution data on commercial drug products can be life-threatening to patients. For example, in a study conducted by Barone *et al.* [13], it was found that among the 25 piroxicam capsule brands sold on the international market, 72 percent failed to meet the USP dissolution test requirements. This indicates possible differences in the formulations of these capsule brands. Moreover, these dissolution failures post a potential difference in bioavailability and bioequivalence. Bioavailability is the amount of drug that enters systemic circulation. Bioequivalence is the equivalent drug concentrations in blood plasma and tissues when drug products are given to the same patient in the same dosage regimen. Consequently, drug efficacy could be altered. In the case of piroxicam, the difference in bioavailability could result in the rare side effect of gastrointestinal bleeding [13, 14]. To maximize patient safety and reduce potential financial burden, proper setup of the dissolution test method during the entire product development process is critical.

1.3 Criteria for Success

A reliable dissolution test method should accurately reveal the performance of a drug product. If the doses or the dissolution rates of two different lots of drug products

are supposed to be different, then the dissolution test method should be able to discriminate between them. Likewise, the test method should provide consistent measurements if the drug products are deemed to be identical.

In an ideal environment, a dissolution test method is considered to be developed once the dissolution medium, the speed of the stirring element, the wavelength to be studied, and the sampling time intervals have been identified. The dissolution medium is selected to allow appropriate sink conditions for dissolution to occur, while the stirring element helps distribute the drug within the medium and mimics the *in vivo* hydrodynamic environment. The wavelength is chosen to detect drug concentration in the medium, and the sampling time intervals are the specific times when the amount of drug dissolved is measured.

Upon developing a test method, the drug product is randomly dropped into the dissolution vessel and its performance appraised. However, it has been reported that the drug product location in the USP Apparatus II dissolution vessel during the test and the speed of the stirring element have substantial influence on the hydrodynamics in dissolution testing [9, 10, 15-18]. The drug product experiences different shear forces and fluid velocities at various locations in the dissolution vessel. Shear force is important in dissolution testing, as it determines the boundary layer for mass transfer of the drug substance from the drug product into the surrounding medium. Lower shear, and hence a slower dissolution rate, is found when the drug product is located at the bottom center of the vessel [9, 10, 15-18]. Different paddle speeds are found to give rise to different fluid flow patterns [9, 10, 15-18]. All these factors shape the dissolution profile and determine

the dissolution result. It is therefore crucial to be able to identify whether the difference in dissolution results is due to drug product variations, or if it is caused by the inherent hydrodynamic variations within the apparatus. To set up reliable test methods and acquire meaningful results, the hydrodynamics of the dissolution process and the interactions between the drug product and the *in vitro* dissolution medium must be fully understood.

1.4 Hydrodynamics and Numerical Simulation of Capsules Dissolution

Interest in understanding the hydrodynamics of the dissolution process has grown in recent years [9, 10, 16-25]. Several numerical simulations of tablet dissolution in the USP Apparatus II dissolution vessel are documented [9, 10, 16-19, 21, 24, 25]. Computational fluid dynamics (CFD) is adopted to model the hydrodynamics of the dissolution apparatus. For example, the effects of paddle speed, impeller clearance, impeller type, vessel geometry, and the position of tablets on the hydrodynamics in the dissolution vessel have been studied [9, 10, 15-19, 21]. The resulting velocity flow fields, as well as the shear environment, are found to be non-uniform [9, 10, 15-19, 21]. These non-uniformities lead to fluctuations in the mass transfer rate of the tablet material to the medium, thus explaining the substantial dissolution variations.

Among the 763 drugs in the FDA database for which recommended dissolution methods are provided, 506 are given in tablet form while 171 are in capsule form [3]. The other 86 drugs are in other dosage forms, such as suspension, injection, or suppository [3]. Capsules are the second most common type of dosage form. However, detailed research of capsule dissolution in the USP Apparatus II is not well reported.

The complex flow field in the dissolution vessel intensifies the need for further research. This study aims to call attention to the influence of hydrodynamics on capsule dissolution. First, a mathematical model that describes the dissolution process via erosion and disintegration was established. The mass transfer coefficient between the dosage and medium was determined both experimentally from dissolution data in the literature, and theoretically with CFD-predicted data. The model was then coupled with predicted mass transfer coefficients to describe the dissolution of a capsule under agitation conditions in a USP Apparatus II dissolution bath. Numerical simulation of the capsule model was conducted using a commercially available numerical computation platform (Microsoft Excel™). Equations that describe the dissolution profile were developed and the simulated profile was verified using the capsules dissolution profiles from published experimental dissolution data. This resulted in a computational model that describes the capsule dissolution process. This model can aid in process optimization and can maximize process development efficiency by allowing the study of a larger sample size in a shorter amount of time (as compared to conducting numerous physical dissolution experiments).

CHAPTER TWO

LITERATURE REVIEW

A good oral drug product is expected to provide both the anticipated therapy and consistent efficacy. Changes in drug substance polymorph (e.g. amorphous or crystalline), formulation differences (e.g. excipients properties), process parameters variations (e.g. tablet hardness), and drug product stability in various environments (e.g. moisture, capsule cross-linking) are some of the factors affecting the effectiveness of the final drug product. Therefore, it is important to identify and to control the source of variability before the drug product is released for human consumption.

By comparing the dissolution profiles of drug products, the existence of any source of variability may be identified. However, many reports in the literature indicated that dissolution variations could be caused by the inherent variability of the dissolution apparatus itself [5, 6, 8-10, 15-17, 21, 23-27]. Tablet or capsule dissolution occurs via a mass transfer process. The velocity flow field that is created by paddle rotation in the vessel affects the mass transfer process. Therefore, it is important to understand both mass transfer and the hydrodynamic conditions in the dissolution apparatus.

This review covers the brief history and importance of *in vitro* dissolution testing, the mass transfer and hydrodynamic effect on tablet dissolution, and a discussion on capsule dissolution. It ends with a summary of previous work and a discussion of how the current research fits into and benefits the study of hydrodynamics in USP dissolution test Apparatus II.

2.1 History and Importance of Dissolution Testing

Noyes and Whitney [28] conducted the first dissolution experiment in 1897. They suggested that dissolution of materials into the surrounding medium was determined in a region where a thin diffusion layer formed around the solid particle. In addition, they showed that the rate of dissolution is proportional to the difference between the saturated solubility, C_s, of the substance and the concentration, C, at time t [28]. Equation 1 presents the statement mathematically, where k_N is the proportionality constant.

$$\frac{dC}{dt} = k_N (C_s - C) \qquad \text{Equation 1}$$

In 1904, Nernst and Brunner explained the rate of drug dissolution as a function of the diffusion coefficient, D_{AB}, the surface area, A, the diffusion layer thickness, h, the dissolution medium volume, V_L, and the concentration difference. The Nernst-Brunner equation is presented in Equation 2 [7, 29].

$$\frac{dC}{dt} = \frac{D_{AB} A}{V_L h} (C_s - C) \qquad \text{Equation 2}$$

It was not until the 1970s that dissolution experiments of pharmaceutical drug products became an official test in the USP. Since then, the USP Apparatus II has been the most common apparatus for solid drug product testing [4, 29]. Dissolution testing has become a regulatory requirement mandated by the FDA. It is required both for the submission of new drug applications (NDAs) for new chemical entities, and for abbreviated new drug applications (ANDAs) for generic products. It is also required for assuring a product's sameness after scale-up or post-approval changes and for waiving

the bioequivalence requirements for lower strengths of a drug product [1]. There is no doubt that dissolution testing plays a very important role in the drug development process, and the information it provides can be critical to the success or failure of a drug product.

There are several reasons that make dissolution testing a prevailing tool and a primary choice in formulation development. First and foremost, the dissolution test is the only *in vitro* test that can help predict *in vivo* performance of a drug product [30]. In simpler terms, it allows drug development scientists to find out if a drug product can dissolve and be bioavailable in the patient. The test is conducted isothermally at body temperature (37°C) and the dissolution medium is prepared to have a similar pH to the pH of the gastro-intestinal tract. If a drug is to be absorbed mainly in the stomach, a dissolution medium of pH 1.2 should be used, whereas if it is to be absorbed mainly in the intestine, the pH of the dissolution medium should be 6.8. The use of surfactant or dissolution medium at other pHs (in the range of 1.2 to 8.0) is sometimes employed upon proper justifications [1]. Some other dissolution testing conditions include the use of 900 mL of dissolution medium to allow adequate sink conditions, and the use of paddle rotation to ensure proper mixing between the "drug-saturated layer of dissolution from around the dosage" and the surrounding medium with a lower drug concentration [30].

With such a critical role in the drug development process, dissolution testing is governed and regulated by both the USP and FDA [1, 2, 3, 30]. The dissolution chapter in the USP has been harmonized internationally with the European Pharmacopoeia and the Japanese Pharmacopoeia [2, 30]. Specifications and tolerances of the dissolution

apparatus are defined and documented in the USP chapter 711 [2]. In addition, the USP describes the use of performance verification tests to determine the suitability of a test assembly, the procedures to conduct dissolution tests for various dosage forms (immediate-release, extended-release, and delayed-released), and the acceptance criteria for dissolution test results [2]. On the other hand, the FDA "reviews the USP monograph dissolution tests for consistency with the dissolution conditions in the approved product's New Drug Application" [30]. It also provides a list of guidance documents for the industry.

2.2 Mass Transfer and Hydrodynamic Effects on Tablet Dissolution

Tablet dissolution is a mass transfer process, wherein a solid mass (comprised of the active pharmaceutical ingredient compacted together with pharmaceutical excipients) starts dissolving into the surrounding medium via an erosion or disintegration mechanism. Tablet mass transfer by molecular diffusion alone would be an extremely slow process. To enhance the mass transfer rate and to ensure proper mixing within the liquid, a paddle rotating at a designated speed is applied during dissolution testing. It is generally assumed that mixing is uniform. However, the fluid velocity distribution in the system, generated from the rotating paddle, may not necessarily be homogeneous. Numerous reports have suggested that the complex hydrodynamics of the dissolution Apparatus II is attributed to the high variability in dissolution test results [9, 10, 15-19, 21, 23-27, 31]. This section reviews the studies conducted through experiments and numerical simulations of fluid motion to understand the mass transfer process and the

hydrodynamics of fluid flow within the dissolution Apparatus II. The effect of hydrodynamics within the vessel on tablet dissolution is also discussed.

2.2.1 Mass Transfer

When a solid tablet is dropped into a liquid dissolution medium, diffusion and mass transfer from the solid to the surrounding liquid take place. This mass transfer process can be described by Equation 3, where C is the drug concentration in the dissolution medium at time t, C_s is the saturated concentration of the drug, k is the mass transfer coefficient, A is the surface area of the solid dosage, and V_L is the volume of the dissolution medium [17]. Equation 3 shows that the rate of drug dissolution is directly proportional to the mass transfer coefficient, tablet surface area, and the concentration gradient.

$$\frac{dC}{dt} = \frac{kA}{V_L}\left(C_s - C\right) \qquad \text{Equation 3}$$

Throughout the tablet dissolution process, a diffusion boundary layer forms around the tablet. As shown in Equation 2, the dissolution rate is inversely proportional to the thickness of the diffusion layer. The thicker the diffusion boundary layer, the slower the mass transfer process. Consequently, the dissolution rate becomes slower. Since the shear force exerted by the fluid can affect the thickness of the boundary layer at the surface of the tablet, any shear rate variation within the dissolution medium can greatly affect the dissolution results [19]. In addition, mass transfer is proportional to the velocity gradient in the boundary layer and the corresponding local strain rate. Therefore, a high strain rate will result in a more rapid dissolution rate. A detailed

understanding of the velocity and strain rate distributions within the vessel fluid is essential to fully evaluate the dissolution process.

2.2.2 Hydrodynamics and Computational Fluid Dynamics

Interest in using CFD to predict fluid motion in a system has grown in recent years. CFD is used to predict velocity, energy, and strain rate patterns. It is also used to provide a visual description of the hydrodynamics of a system through the interpretation of numerical data, using appropriate graphing routines. Numerical simulations enable the study of systems where it is impossible or very challenging to measure these values quantitatively via experimental methods. In addition, CFD allows for faster and less expensive simulation of experiments. In studying the hydrodynamics of tablet dissolution, many researchers have adopted this technique to simulate the fluid flow conditions inside the vessel [9, 16-25, 27, 31, 32].

The CFD simulation of fluid flow conditions in the USP Apparatus involves solving the governing equations that describe fluid motion. According to the set-up of the apparatus, cylindrical coordinates are used to model the system. These include the continuity equation and the Navier-Stokes equations, which are presented in Equations 4 and 5, respectively [25, 33, 34]. The continuity equation is a mathematical expression of the conservation of mass that describes the time rate of change of fluid density at a certain point in space. Assuming the dissolution medium is incompressible, the time rate of change of fluid density equals zero. The Navier-Stokes equations refer to the conservation of momentum. Since the dissolution testing is conducted isothermally at 37°C, the energy equations are not included in this study.

$$\frac{\partial \rho}{\partial t} + (\nabla \cdot \rho \boldsymbol{v}) = 0 \qquad \text{Equation 4}$$

$$\rho \frac{D\boldsymbol{v}}{Dt} = -\nabla p + \mu \nabla^2 \boldsymbol{v} + \rho \boldsymbol{g} \qquad \text{Equation 5}$$

The first term of the continuity equation in Equation 4 describes the rate of change of mass per unit volume, while the second term describes the net rate of change of mass per unit volume, and the sum of these terms should equal to zero. For dissolution study, it is assumed that there is no reaction between the drug product and dissolution medium. Therefore, no reaction term is required. In this continuity equation, ρ is the density of the fluid, t is time, and $\boldsymbol{v}$ represents the velocity vector with components v_r, v_θ, and v_z in the radial, tangential, and axial directions, respectively. As presented in Equation 5, the conservation of momentum includes convective transport, molecular transport, and external force such as gravitational force. These are described by the term on the left, the first and second terms on the right, and the third term on the right of the equation, respectively. This Navier-Stokes equation is presented in material derivation form, where $\boldsymbol{v}$ represents the velocity vector with the components v_r, v_θ, and v_z, p is the fluid pressure, μ is the dynamic fluid viscosity, and $\boldsymbol{g}$ is the gravitational acceleration vector.

In addition to the governing equations, dimensionless parameters such as Reynolds number are often used to characterize fluid flow. As presented in Equation 6, Reynolds number, Re, is the ratio of inertial to frictional forces in a fluid system, where ρ is the fluid density, N is the rotational speed of the agitator, d is the agitator diameter, and μ is the dynamic fluid viscosity [9, 23, 31, 34]. Fluid flow can be categorized into three

different regimes: a laminar regime as indicated by a small Reynolds number, a turbulent regime with a large Reynolds number, and a transitional regime that is between the laminar and turbulent regimes. In the case of mixing tanks, the transitional regime is characterized by Reynolds numbers between 50 and 5000 [34].

$$\mathrm{Re} = \frac{\rho N d^2}{\mu} \qquad \text{Equation 6}$$

According to the FDA industry guidelines, dissolution testing using the Apparatus II should be conducted under mild (non-fully turbulent) conditions, with a paddle rotation speed of 50 rpm or 75 rpm [1]. Bai *et al.* [24] mentioned that at a low impeller Reynolds number of 4939 with a corresponding agitation speed of 50 rpm, most of the fluid in the vessel is in a transitional domain. Similarly, Kukura *et al.* [31] show that under standard operating conditions where the Reynolds number is approximately equal to 5000, the flow within the Apparatus II is in a transitional turbulence regime. This transitional regime creates an unstable environment that makes the flow behavior of the fluid in the vessel and around the tablets highly time-dependent [23, 31]. The substantial variation in hydrodynamics of the Apparatus II could therefore be attributed to the Reynolds number, a characteristic of the flow field during dissolution testing.

According to the literature, to model the fluid velocity in the dissolution vessel using CFD, the flow volume is first discretized into a mesh of finite elements where the velocity for each node was solved using the governing equations [9, 16, 17, 19, 21, 23, 24]. Due to the geometry of the dissolution vessel, the cylindrical portion of the vessel was meshed with hex cells, while the lower hemispherical portion of the vessel was

meshed with unstructured tetrahedral cells [17, 24]. These meshes were further refined until the simulation converged to a stable solution. Having the impeller rotated at 50 rpm, Bai *et al.* [17, 21, 24] showed that the k-ω model with a low Reynolds number correction was a better turbulence model to predict the fluid velocity than other models. This was confirmed by comparing the CFD predicted values to the experimental velocity data obtained via laser-doppler velocimetry [24]. Baxter *et al.* [9, 19] and Kukura *et al.* [16, 23], however, incorporated the Reynolds-averaged Navier-Stokes (RANS) equation to the CFD model and treated the fluid flow in the turbulent regime.

While constructing the mathematical model, a no-slip condition was assumed at all solid surfaces [17, 21, 24]. In addition, the air-water interface was modeled as a flat frictionless surface. The normal gradients of all the variables are therefore equal to zero at the air-water interface. In the model developed by Bai *et al.* [17, 21, 24], the vessel wall and the tablet were assumed to be rotating, while the impeller was set as stationary. The result of this simulation using the CFD solver (Fluent) showed the 3-dimensional velocity and strain rate distributions within the dissolution vessel.

After the CFD solver generates the velocity or strain rate data for the selected flow field, the information is compared to the experimental data to validate the model. Figure 2 presents the velocity field pattern inside the dissolution apparatus at 50 rpm. The velocity field pattern shows two recirculation loops, one above and one below the impeller [9, 16, 21]. For the loop above the impeller, fluid is ejected up the vessel wall from the impeller. Upon reaching the surface of the liquid, the fluid moves down along a path that is located between the shaft and the wall. For the loop below the impeller, fluid

moves down along the vessel wall towards the base of the vessel, and moves back up towards the bottom of the impeller. The velocity flow field predicted by Bai *et al.* [17, 21, 24] showed that the recirculation loop was not able to penetrate a core region along the vessel base below the impeller.

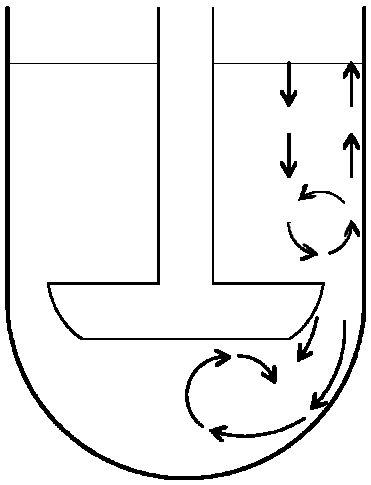

Figure 2. Velocity field pattern inside Apparatus II at 50 rpm.

The velocity pattern inside the Apparatus II appears to be highly heterogeneous. Velocity decays rapidly as it moves away from the impeller blades [21]. A review of the hydrodynamic conditions reported by various researchers showed that there is generally a low velocity region below the center of the paddle, where the solid dosage is likely to be located [20, 21, 24, 25, 27]. Figure 3 presents the velocity flow field in the vessel with the presence of a tablet [35]. The figure shows that the velocity around the tablet is a lot lower compared to the non-centrally located positions. D'Arcy *et al.* [20] modeled the paddle apparatus and found that when the paddle rotates at 50 rpm, the velocity of the fluid within 12 mm of the center at the base of the vessel was about 0.8×10^{-3} m/s. However, velocity had a much wider range throughout the base of the vessel, which

varied from 0.8×10^{-3} to 79.6×10^{-3} m/s. In another study conducted by D'Arcy *et al.* [27], the dissolution rate was found to agree with the CFD data, where both dissolution rate and velocity increased significantly when the solid dosage was moved from the center of the vessel to 13 mm away from the center. Bai *et al.* [21] also found that the velocity of a 10-mm-wide region between the bottom center of the impeller and the bottom center of the vessel is less than 5% of the impeller tip speed. This region accounted for the lowest fluid velocity region within the entire vessel [21, 24]. Indicated both numerically by CFD simulation and experimentally by laser-doppler velocimetry, the flow in this region is mainly dominated by weak tangential velocities (velocity component in the direction of paddle rotation) and is nearly stagnant in the vertical plane [24].

Similarly, McCarthy *et al.* [25] found that the velocity distribution within the vessel was highly variable. The authors showed that the region below the center of the impeller contained a low velocity domain, and the fluid velocity at the base of the vessel where the solid dosage is likely to be located varied significantly within regions that were 8 to 10 mm apart. These results explain the variations often observed in dissolution testing. In addition, they correlate well with other work cited in the literature, which show that slight differences in the position of a tablet during dissolution testing can lead to substantial variation in dissolution results [9, 10, 15-17, 27].

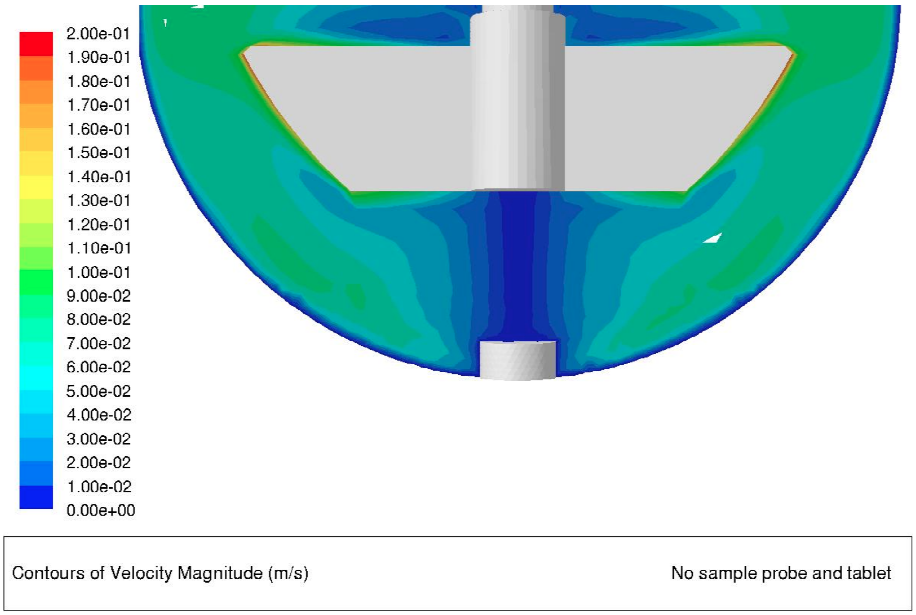

Figure 3. Velocity flow field inside a paddle apparatus with a tablet [35] (reprinted with permission from O. Akiti).

Some researchers further evaluate the magnitude of the tangential velocity as a function of radial position in the region below the paddle [24, 25]. The tangential velocity component of the velocity was predominant, compared to the axial and radial components throughout the vessel [24, 25]. Figure 4 presents the cylindrical velocity components. Bai *et al.* [24] showed that in the region below the impeller, the tangential velocity increased radially to a peak velocity before its magnitude reduced again as it approached the vessel wall. Compared to the region above the impeller, the peak tangential velocity was closer to the wall when it was below the impeller, although the velocity eventually decayed in both regions. McCarthy *et al.* [25] also studied the tangential velocities that are 5.3 mm from the base of the vessel at a paddle speed of 50 rpm. Similar to Bai *et al.* [24], they found that the tangential velocity increased as the

radius increased from about 5 mm to 17 mm, although tangential velocity at a radius beyond 20 mm was not measured.

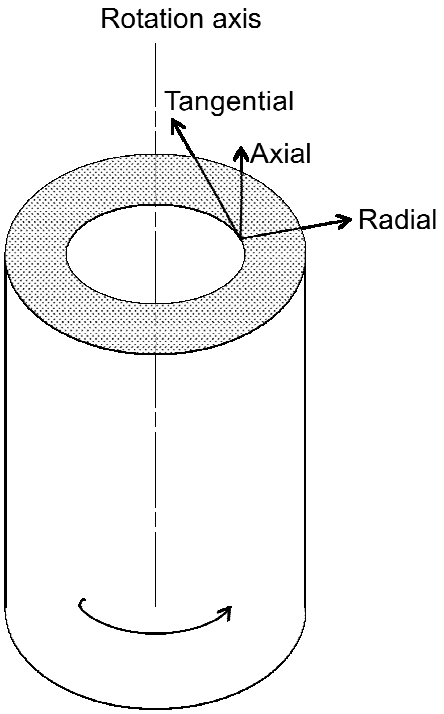

Figure 4. Cylindrical velocity components.

Bai *et al.* [24] graphically presented CFD-predicted tangential velocity profiles on different iso-surfaces, or horizontal planes, located at various vertical positions along the height of the vessel when the paddle rotated at a speed of 50 rpm (corresponding to 0.194 m/s impeller tip speed). The computation approach to determine tangential velocities from the graphs generated by Bai *et al.* [24] can be found in Appendix A. The resulting computed tangential velocities on various iso-surface planes below the paddle, together with the corresponding distance from the bottom of the vessel, are tabulated in Table 1. Note that the tangential velocities presented in Table 1 correspond to a radial distance of approximately 5 mm to 10 mm from the center of the impeller, equivalent to a 10 mm to

20 mm diameter circle (as shown in Figure 5) where a solid dosage is most likely to be located. To help visualize the various locations of iso-surface plane, Figure 5 also presents the relative distances between the bottom of the paddle and the bottom of the vessel.

Table 1. Tangential velocity at various distances from the bottom of the vessel (5 to 10 mm from the center of the impeller) [24].

Distance from vessel bottom (mm)	v_θ (m/s)
19.05	~ 0.029 – 0.058
13.05	~ 0.031 – 0.058
7.05	~ 0.029 – 0.056

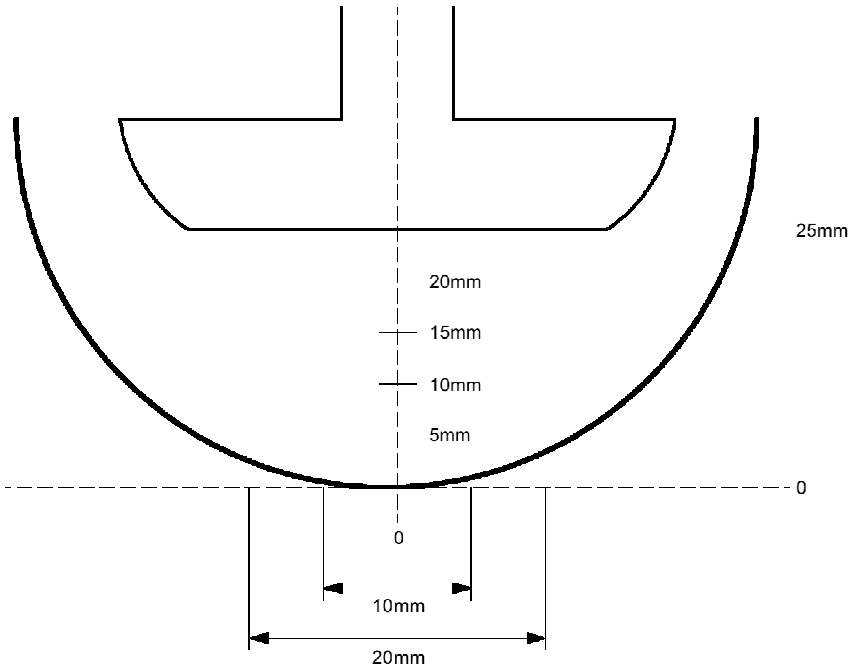

Figure 5. Radial distance from the shaft and various locations of the iso-surface plane.

To compare the tangential velocities obtained by Bai *et al.* [24] and McCarthy *et al.* [25], the radial distances and tangential velocities presented in Table 2 are estimated from graphical data presented by McCarthy *et al.* [25]. Similarly, the computational

approach towards obtaining the tangential velocities from McCarthy *et al.* [25] can be found in Appendix A. Tangential velocities estimated from both sources (as shown in Tables 1 and 2) compare well at a radial distance of about 5 mm to 10 mm. Table 3 presents the CFD-predicted velocity vectors, which consist of the radial, tangential, and axial velocity components, around the tablet surface location from the literature reviewed in this section. The tangential velocities calculated in both Tables 1 and 2 are within the same order of magnitude as the CFD-predicted velocity vectors in Table 3, indicating that the tangential velocity plays a major role in predicting CFD velocity [24, 25].

Table 2. Tangential velocity at various radial distances from the center of the shaft (5.3 mm from the base of the vessel) [25].

r (mm)	v_θ (m/s)
4.78	0.029
8.99	0.049
13.31	0.069
17.48	0.088

Table 3. CFD-predicted velocity vectors around the tablet surface location.

Description	CFD-predicted velocity vectors (m/s)	Ref.
No tablet	~ 0.03 – 0.06	[17]
	~ 0.01 – 0.04	[21]
	~ 0.01 – 0.05	[24]
Centrally located tablet (erosion)	~ 0.04 – 0.06	[17]
Centrally located tablet (disintegration)	~ 0.03 – 0.06	[17]
Centrally located tablet	~ 0.012 – 0.024	[27]

In addition to predicting velocity profiles and estimating the tangential velocity using CFD, Bai *et al.* [17] further utilized the CFD-predicted tangential velocity to computationally determine the mass transfer coefficient for a centrally located non-disintegrating salicylic acid tablet. First, the mass transfer coefficients for both the top

surface and the side of a tablet were estimated. Assuming that the mass transfer process at the top of the surface resembles that of a rotating disk, while the mass transfer process on the side of the tablet is similar to that of a rotating cylinder surrounded by fluid, the mass transfer coefficients for these two locations can be described by Equations 7 and 8 [17, 36, 37]. Here, k_{top} is the mass transfer coefficient on the top of the tablet, D_{AB} is the diffusivity or diffusion coefficient between the solute and the solvent, ν is the kinematic viscosity of the liquid, ω is the angular velocity of the rotating disk, k_{side} is the mass transfer coefficient on the side of the tablet, d_T is the diameter of the tablet, Re_Ω is the rotating Reynolds number, and Sc is the Schmidt number. The overall theoretical mass transfer coefficient for the entire tablet can then be estimated according to Equation 9, where A_{top} and A_{side} refer to the surface area of the top and the side of the tablet, respectively [17]. Dissolution of tablets was also conducted to calculate the mass transfer coefficient experimentally by integrating the mass transfer equation presented in Equation 3. The theoretically predicted mass transfer coefficient was found to correlate well with the experimental mass transfer coefficient. In addition, mass transfer coefficients for tablets located at various off-centered positions were also estimated and the resulting values were found to agree with the CFD-predicted strain rate as well as the dissolution results.

$$k_{top} = 0.62 D_{AB}^{2/3} \nu^{-1/6} \omega^{1/2} \qquad \text{Equation 7}$$

$$\frac{k_{side} d_T}{D_{AB}} = 0.135 \left[0.5 \mathrm{Re}_\Omega^2 Sc \right]^{1/3} \qquad \text{Equation 8}$$

$$k = \frac{k_{top}A_{top} + k_{side}A_{side}}{A_{top} + A_{side}}$$ Equation 9

Strain rate is another valuable piece of information predicted by CFD to help understand the hydrodynamic conditions within the dissolution vessel. A high strain rate environment corresponds to faster drug product dissolution, while a low strain rate gives a slower dissolution profile. To find out the strain rate distribution, Baxter *et al.* and Kukura *et al.* [9, 16] developed a model for the Apparatus II operated at both 50 rpm (Reynolds number of 4688) and 100 rpm (Reynolds number of 9375). The model shows that the spatial distribution of shear rates within the vessel is substantially heterogeneous. A low-shear region is identified at the bottom center of the vessel (where a tablet will be located), while a two-fold increase in shear force is found 21 mm from the center. Experiments where the physical locations of the tablets are controlled showed the substantial variability in dissolution rates. The two-fold increase in shear force on the tablet, with respect to the location of the tablets in the vessel, was also found to affect the corresponding dissolution rate. These results confirm the heterogeneous shear environment as revealed by the model. Bai *et al.* [21], who found that a 10-mm-wide core (located below the impeller shaft) with low strain rates was surrounded by a region of high strain rates, also showed that the strain rate distribution is highly heterogeneous along the bottom of the vessel. In addition, Bai *et al.* [17] showed the strain rate variation through CFD simulation and dissolution studies. The authors showed that the centrally located tablets had both the slowest dissolution profiles and the lowest strain rate on their surfaces, which agrees with the prediction of the CFD model.

The literature review showed that both the mass transfer process and the hydrodynamic conditions within the dissolution medium govern the dissolution of a solid dosage. CFD simulation shows that both the velocity and strain rate distributions within the USP Apparatus II are highly heterogeneous, with a region of low velocity and low strain rate below the paddle [9, 16, 17, 20, 21, 24, 25, 27]. In addition, the pronounced changes in velocity magnitude over short distances, especially near the vessel base where tablets are likely to be located during dissolution tests, may contribute to the variability found in dissolution testing [9, 10, 15-17, 27]. Finally, it has been shown that information generated by CFD not only correlates with experimental results, the data obtained can also be used to determine tablet mass transfer coefficient data [17].

2.3 Capsule Dissolution

The hydrodynamic environment within the dissolution Apparatus II described in Section 2.2 was evaluated either with a tablet or without any pharmaceutical dosage form. Although not much attention has been paid to the effect of hydrodynamics on capsule dissolution, this should not undermine the importance of capsules in delivering pharmaceutical drug substances.

The capsule is the second most popular type of pharmaceutical dosage form. It allows convenient, direct filling of powdered materials and provides taste masking. Unlike a tablet, which is a one-piece solid dosage form, pharmaceutical substances delivered in capsules consist of two separable parts: the capsule shell and the filling. Depending on the filling inside the capsule, the manufacturing process of a capsule drug product can be much simpler than that of a tablet drug product. However, owing to the

ability of capsules to encapsulate a variety of substances such as powders, granules, pellets, slugs, tablets, semi-solids, liquids, or even a combination of these materials, capsule dissolution can be more complex than tablet dissolution. Usually, hard capsules are used to encapsulate solid materials while soft capsules are used for liquids or semi-solids [38]. However, hard capsules are occasionally filled with liquids as well.

There are three common types of hard capsule shell materials used in practice: gelatin, hydroxypropyl methylcellulose, and gelatin/polyethylene glycol [39, 40]. Among them, gelatin has the longest history in hard capsule shell manufacturing due to its use in the food industry. Gelatin is soluble in biological fluids and it forms films very easily. However, it also possesses some undesirable properties, such as brittleness and cross-linking formation when the shell is exposed to hygroscopic materials or materials with aldehyde groups [39, 41]. Gelatin, water, and coloring agents are the ingredients used in forming hard gelatin capsules.

A capsule itself consists of two portions: the longer part is called the capsule body and the shorter part is called the capsule cap. Hard gelatin capsules are available in a variety of sizes that can range from size 000 (largest) to size 5 (smallest) [42]. The size of the capsule chosen depends on the amount and the density of materials it needs to hold. Table 4 presents the capacities and dimensions of size 0 and size 1 capsules, which are commonly used in pharmaceutical products. Based on the external diameters of the capsule, the thickness of the capsule shell is probably less than or around 0.15 mm. Figure 6 presents the exterior view of a capsule shell as well as the interior (filled with a slug) before and after the cap is snapped shut.

Table 4. Capacities and dimensions of size 0 and size 1 capsules [42].

Size	0	1
Capacity—volume (mL)	0.68	0.50
Capsule body length (mm)	18.44 ± 0.46	16.61 ± 0.46
Capsule cap length (mm)	10.72 ± 0.46	9.78 ± 0.46
External body diameter (mm)	7.34 ± 0.06	6.63 ± 0.06
External cap diameter (mm)	7.64 ± 0.06	6.91 ± 0.06
Overall closed length (mm)	21.7 ± 0.3	19.4 ± 0.3

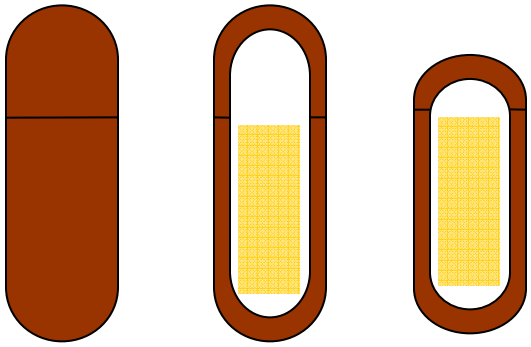

Figure 6. Different views of a capsule (left: exterior; middle: interior; right: interior after cap is snapped shut).

To understand the process of capsule dissolution where a drug is being released from the capsule, capsule shell dissolution needs to be addressed. During capsule shell dissolution, tiny holes form and grow into openings big enough to release the encapsulated materials into the dissolution medium. Chiwele *et al.* [39] studied the shell dissolution time for several types of sizes 0 and 3 hard capsules. They found that for hard gelatin capsules, the shoulder of the round ends, which are the weakest points of the capsules, dissolved first. In addition, at 37°C, gelatin capsule shells dissolved within 300 seconds in all the dissolution media (water, hydrochloric acid, phosphate buffer, artificial gastric juice, or artificial intestinal juice) investigated in their studies. El-Malah *et al.*

[41] conducted a similar study to determine the hard gelatin capsule shell rupture time for sizes 00, 0, 1, and 3 capsules. They found that the hard gelatin capsule shell took about 1.1 minutes to 2.1 minutes before the fill materials inside the capsule were released into the dissolution medium (simulated gastric fluid, simulated intestinal fluid).

It might appear that the capsule shell needs to be completely dissolved before drug dissolution takes place. However, these two processes, shell dissolution and drug dissolution, in fact overlap each other [39-41]. Upon the formation of a tiny hole on the capsule shell, the mass transfer process between the drug and the surrounding medium begins. Water is drawn into the capsule body while the encapsulated materials (drug and excipients) are continuously released.

Melia *et al.* [38, 43] stated that the drug is released from the capsule via two main processes: disintegration and dissolution. They described disintegration as "the rapid fragmentation of the dosage form under the action of the disintegrant" [38]. Disintegration reduces the size of the material by breaking it into smaller portions. Dissolution, on the other hand, refers to the process where a solid dissolves into a liquid. The disintegration process usually completes before the dissolution process, although the two processes take place simultaneously at the beginning of the dissolution process [38, 44]. While drug dissolution is mainly driven by the disintegration process, in some cases where the encapsulated materials do not disintegrate, drug dissolution can be driven by an erosion process that is similar to the non-disintegrating tablets [17]. This implies that the encapsulated material reduces in size because of material wearing from the surface. The

drug release process from a capsule dosage form where a slug is the encapsulated material is summarized in Figure 7 as a schematic diagram.

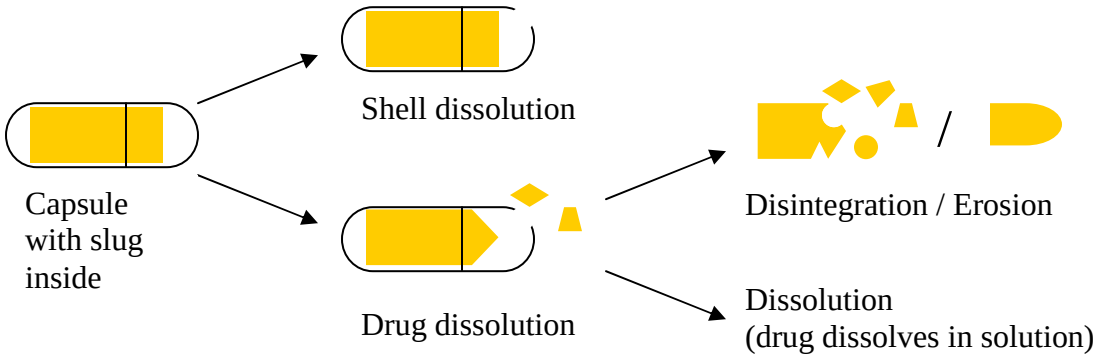

Figure 7. Drug release process from capsule dosage form.

In general, capsule dissolution (drug release process) refers to the capsule shell dissolution and the filling contents (drug) dissolution through the disintegration or erosion process. However, as stated earlier, detailed research of capsule dissolution with the hydrodynamic effect in the dissolution Apparatus II is not well reported. Consequently, it was the intention of this research to study capsule dissolution by incorporating some of the materials that are already examined in the literature for tablet dissolution.

2.4 Summary of Literature Review

In summary, the heterogeneous hydrodynamic environment within the USP Apparatus II has been reported by numerous researchers [9, 16, 17, 20, 21, 24, 25, 27]. Also, CFD simulations of Apparatus II with and without tablets were presented, along with the corresponding hydrodynamic effect on tablet dissolution [9, 16, 17, 20, 21, 24,

25, 27]. These studies, however, did not evaluate the capsule dissolution process in the USP Apparatus II. More specifically, the previous work did not establish a mathematical expression to predict capsule dissolution.

Therefore, one of the goals of this work is to predict the mass transfer coefficient of a slug inside the capsule theoretically as well as from existing experimental data. The CFD-predicted tangential velocity within the dissolution vessel and the predicted mass transfer coefficients were then used to build a model describing the capsule dissolution process via commercially available numerical software.

CHAPTER THREE

RESEARCH HYPOTHESIS AND OBJECTIVES

Previously, it was reported that the hydrodynamic field within the USP Apparatus II was highly heterogeneous. CFD simulations revealed that there was a low velocity region at the vessel bottom, where a tablet was likely to be located. Additionally, the tablet mass transfer coefficient predicted from experimental results correlated well with the theoretical mass transfer coefficient estimated from CFD-predicted tangential velocity. These studies, however, did not evaluate the dissolution process when capsule, the second most common type of drug dosage form, is considered.

The hypotheses of this study were:

1. The capsule slug mass transfer coefficient could be predicted in a manner analogous to the tablet mass transfer coefficient, using a previously determined CFD-predicted tangential velocity.
2. The experimental and theoretical predicted capsule slug mass transfer coefficients could be used in a computational capsule dissolution model to generate a dissolution profile that would be statistically similar to the published experimental dissolution results.

The primary objective of this research was to develop a mathematical model that incorporates mass transfer principles and hydrodynamic effects when describing the capsule dissolution process. This included capsule shell erosion, slug erosion, and slug disintegration. The secondary objective was to determine if the theoretically predicted

mass transfer coefficient for the capsule slug using the CFD-predicted tangential velocity correlated with the mass transfer coefficient predicted from experimental data. Finally, this research aimed to determine if the theoretical and experimental mass transfer coefficients could be incorporated into the capsule model to numerically simulate dissolution profiles that are statistically similar to the published data.

Since the CFD-predicted velocity vectors around the tablet surface location were similar with or without a tablet in the vessel, the hydrodynamic effects on a tablet should be similar to that on a capsule. Therefore, the CFD-predicted tangential velocity can be used to determine the theoretical mass transfer coefficient for a capsule. This embeds the hydrodynamic effects on a capsule within the mass transfer coefficient. In addition, the mass transfer coefficient directly affects the dissolution profile. Therefore, the simulated profiles were statistically compared to the published data to determine the validity of both the model and the value of the mass transfer coefficient.

CHAPTER FOUR

MODEL DEVELOPMENT

The goal of this project was to develop a mathematical model that describes the capsule dissolution process in the USP Dissolution Apparatus II using basic mass transfer principles with the incorporation of vessel hydrodynamics. This involved the development of a mathematical model to describe the capsule dissolution process, the estimation of the mass transfer coefficient to determine the rate of material transfer from the capsule into the bulk fluid, and the numerical simulation of the capsule dissolution profiles. The simulated profiles were then compared with published experimental data to validate the model. The overall model development process is presented as a flow chart in Figure 8.

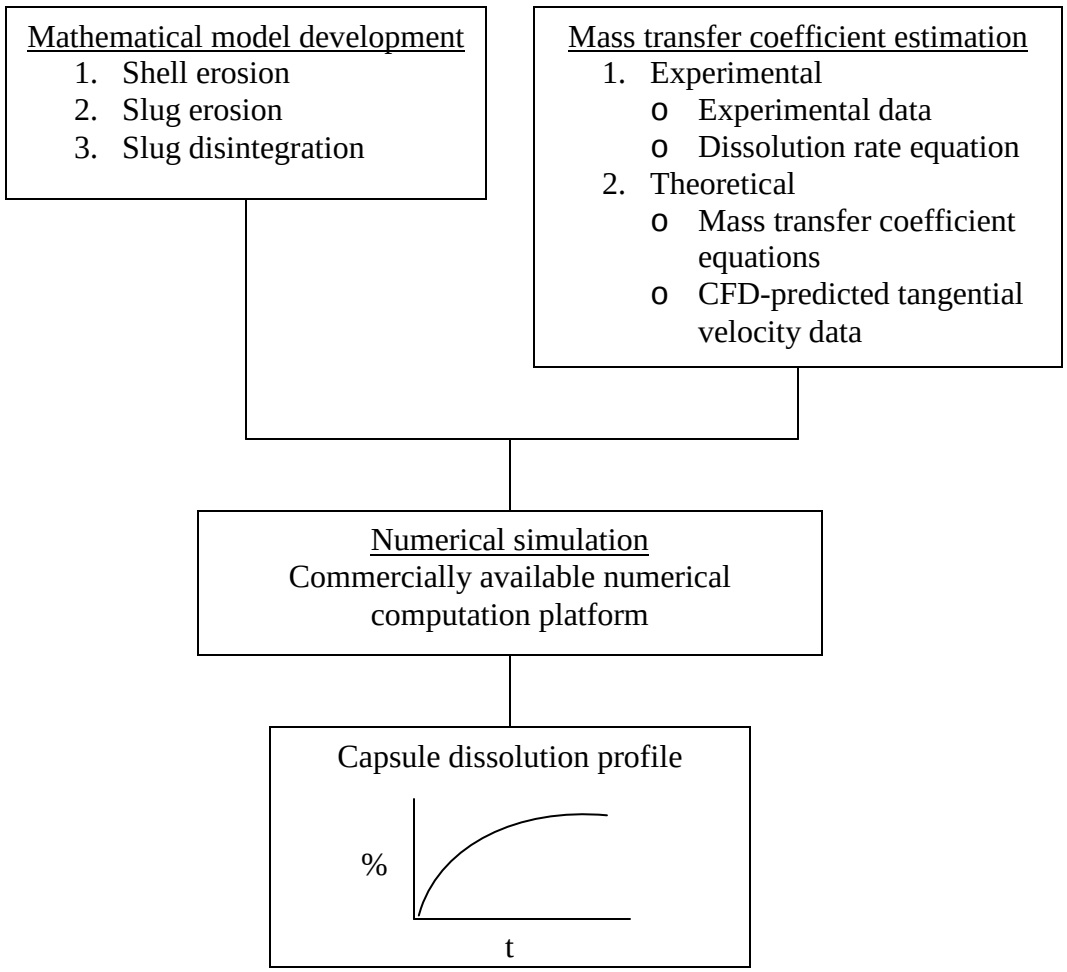

Figure 8. Flow diagram for capsule dissolution profile model development.

As shown in Figure 8, a mathematical model was first developed using basic mass transfer principles. The model describes the capsule shell erosion, slug erosion, and slug disintegration processes. The mass transfer coefficient was determined both experimentally and theoretically. The experimental mass transfer coefficient was estimated using experimental data published in the literature, while the theoretical mass transfer coefficient was calculated from CFD-predicted tangential velocity data. These mass transfer coefficients were incorporated into the mathematical model to numerically

simulate the capsule dissolution profile. The model was validated by testing it with three extreme dissolution scenarios. These scenarios are the pure erosion process, the fast disintegration process, and the pure disintegration process without diffusion. The validity of the model was further evaluated by comparing the simulated dissolution profile with published experimental dissolution profile data. The goodness of fit between the model and the experimental data was assessed statistically by the similarity factor.

4.1 Mathematical Model Development

A mathematical expression that models the capsule dissolution process should describe the mass transfer processes of both the capsule shell and the material that resides within the capsule. The model in this research was based on modeling the capsule contents as a slug inside a hard gelatin capsule. This model was specifically developed for a slug of ascorbic acid with 0.5% magnesium stearate inside a size 1 hard gelatin capsule dissolving in a USP dissolution Apparatus II at 50 rpm in 1000 mL 0.1 N HCl at 37°C. The dissolution experiment data used to assess the model validity were obtained from the work conducted by Heda *et al.* [45].

A slug is a lightly tamped mass of solid material. To form a slug, the drug substance or material blend is machine-tamped into a cylindrical mass. The resulting mass of material resembles a tablet. It is less compacted and has lower hardness than a traditional pharmaceutical tablet. Since the slug resides inside the capsule, its dimensions cannot be larger than the selected capsule size. More precisely, the slug must be shorter than the length of the capsule body for the capsule cap to be snapped shut. In this study, it was assumed that the capsule body was completely filled with the slug material.

Therefore, the length of the slug was equal to 16.46 mm, while the diameter was equal to 6.3 mm. These dimensions were determined by subtracting the thickness of the capsule shell from the dimensions of the capsule body.

Since the capsule dissolution process involves the dissolution of both the capsule shell and the slug it contains, the model was divided into two parts to properly describe both dissolution processes. The capsule shell dissolution was modeled as an erosion process. The mass transfer process for the slug, on the other hand, was modeled in two ways—as a disintegration process and as an erosion process. Both of these processes were evaluated when developing the mathematical model, and then compared to determine which process better described the slug dissolution process. Additionally, the mathematical model assumed that the capsule shell dissolution and slug dissolution occurred in a sequential fashion.

4.1.1 Slug Dissolution Model Development

During the slug dissolution process, mass transfer from the solid drug to the surrounding fluid occurs across a thin layer known as the diffusion layer. The thicker the diffusion layer, the slower the mass transfer or dissolution process. Each system has its own distinct diffusion coefficient that drives the rate of mass transfer. The diffusion coefficient, D_{AB}, or diffusivity, is a function of the properties of the fluid (molecular weight, M, viscosity, μ, association parameter, ψ_B), the molar volume, V_A, of the solute at its normal boiling point, and the temperature, T_K, of the system. Equation 10 describes the Wilke-Chang diffusivity correlation for estimating the mass transfer coefficient [46].

$$D_{AB} = 7.4 \times 10^{-8} \frac{\sqrt{\psi_B M} T_K}{\mu V_A^{0.6}}$$ Equation 10

In addition to the thickness of the diffusion layer and diffusivity, the rate of mass transfer is also affected by the concentration gradient across the diffusion layer and the surface area of the slug. This is described by Equation 11, where m is the mass of the drug diffused into the fluid and A is the surface area of the slug. Since the volume of the fluid (dissolution medium) remains constant throughout the test, applying the law of conservation of mass to the system results in Equation 12 [47]. Combining Equations 11 and 12, the Nernst-Brunner equation (that was presented by Equation 2 in Section 2.1) is obtained. The mass transfer coefficient, k, represents the thickness of the diffusion layer and diffusivity terms in Equation 2, and, when substituted into Equation 2 in Section 2.1, results in Equation 3 in Section 2.2.

$$\frac{dm}{dt} = \frac{D_{AB}}{h} A(C_s - C)$$ Equation 11

$$\frac{dC}{dt} = \frac{1}{V_L} \frac{dm}{dt}$$ Equation 12

To obtain an equation that describes the concentration of drug as a function of time, Equation 3 is integrated by assuming that the mass transfer coefficient remains constant while the surface area of the slug changes with time. This yields Equation 13, which is a general form of the mass transfer equation that describes the amount of drug dissolved per unit volume at a given time t.

$$C(t) = C_s \left\{ 1 - \exp\left[-\frac{k}{V_L} \int_0^t A(t) dt \right] \right\}$$ Equation 13

Before determining a mathematical expression for A(t), the change in the overall surface area as a function of time for a disintegration process, the slug breakage mechanism needs to be defined. Figure 9 presents a schematic diagram that shows a slug that is broken into a portion known as the unbroken slug as well as some disintegrated particles. To simplify the formulation of the problem, the cylindrical slug was modeled as a sphere with its equivalent initial volume. This allows for the surface area and the volume of the slug to be determined directly from the radius using the spherical model, resulting in a one-parameter model. A cylindrical model requires both the dimensions of the radius and the length of the cylinder to determine the surface area and volume of the slug, rendering the model development and subsequent mathematical expressions significantly more complex. This spherical slug was thus assumed to break into an unbroken portion and some disintegrated particles, where the involved particles were assumed to be spherical in shape. These are collectively presented in Figure 9.

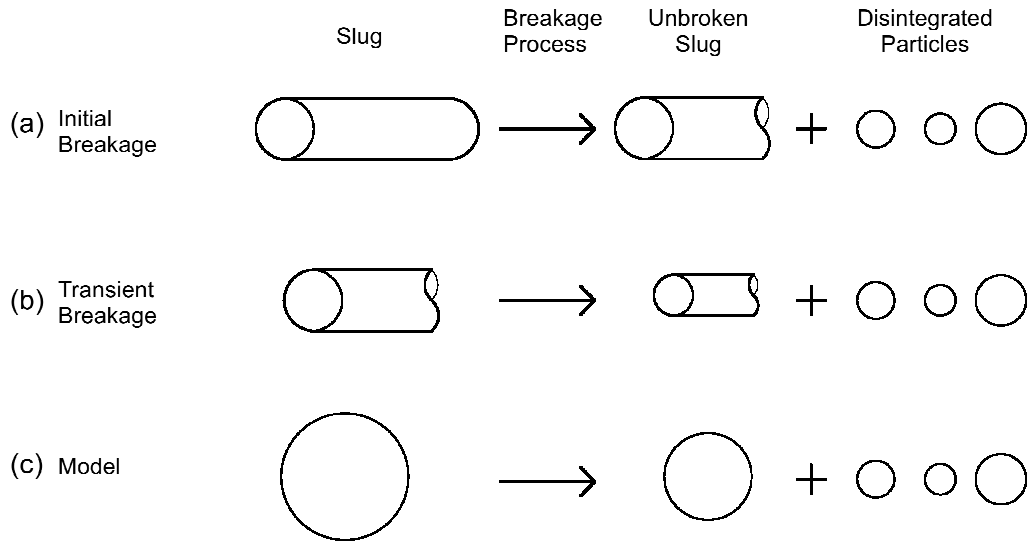

Figure 9. Schematic diagram of the slug disintegration process ((a) initial breakage, cylindrical shape. (b) transient breakage, cylindrical shape. (c) spherical model breakage).

In addition to adopting a spherical model for the dissolution model development, the following assumptions were also made:

- The dissolution medium was well-mixed.
- The initial concentration of dissolved drug in the medium was zero.
- The mass transfer coefficient was independent of time, slug surface area, and disintegrated particles surface area.
- The slug was composed of spherical particles with discrete sizes.

As described in Figure 9, the slug disintegration process consists of two breakage processes: the breakage of the parent slug into a new, smaller unbroken slug; and the generation of disintegrated particles that may break apart further into smaller particles. The breakage of the parent slug into a new, smaller unbroken slug, which is the size reduction of the slug as a function of time, was assumed to follow an exponential decay

described by Equation 14. Here, $r_{Sl,b+1}$ is the radius of the unbroken slug at time t_{b+1}, ρ_{Sl} is the density of the slug that was assumed to be constant, and $r_{nSl,b}$ is the radius of the slug after diffusion at time t_b. Additionally, γ is the disintegration constant or slug breakage coefficient defined in this study. The magnitude of the slug breakage coefficient has a direct impact on the rate of the slug disintegration during the dissolution process. Note that initially at time zero, $t_{b+1} = t_0$ and $r_{Sl,b+1} = r_{nSl,b} = r_{Sl,0}$, which is the initial radius of the slug. Accordingly, the surface area, $A_{Sl,b+1}$, and volume, $V_{Sl,b+1}$, of the unbroken slug can be found at each time interval, as described by Equations 15 and 16.

$$r_{Sl,b+1} = r_{nSl,b} \exp\left(-\frac{\gamma w_\theta}{\rho_{Sl}} t_{b+1}\right) \qquad \text{Equation 14}$$

$$A_{Sl,b+1} = 4\pi r_{Sl,b+1}^2 \qquad \text{Equation 15}$$

$$V_{Sl,b+1} = \frac{4}{3}\pi r_{Sl,b+1}^3 \qquad \text{Equation 16}$$

Once the volume of the unbroken slug is determined, the total volume of the freshly disintegrated particles from the slug at time t_{b+1}, $V_{p,b+1}$, can be obtained. The volume of the leftover particles, $V_{Lp,b+1}$, which equals the volume of the undissolved particles, $V_{np,b}$, that did not dissolve at time t_b, can then be obtained. These are described by Equations 17 and 18, respectively, where $V_{nSl,b}$ is the slug volume after dissolution at time t_b. At time $t_{b+1} = t_0$, $V_{nSl,b}$ equals the initial slug volume, $V_{Sl,0}$. Initially, $V_{np,b}$ equals zero as no disintegration has taken place. However, at any time t_b other than t_0, the drug concentration, C(t), in the dissolution medium must be determined using Equation 13 before the values for $V_{nSl,b}$ and $V_{np,b}$ can be calculated. The surface area expression, A(t), needs to be established first.

$$V_{p,b+1} = V_{nSl,b} - V_{Sl,b+1}$$ Equation 17

$$V_{Lp,b+1} = V_{np,b}$$ Equation 18

Once the expression for the surface area is known, the drug concentration in the dissolution medium at each time, t_b, can be determined. Therefore, the volume of the sample dissolved, $V_{dif,b}$, at each time, t_b, can be computed according to Equation 19. Subtracting the volume of the dissolved material from the initial slug volume, the volume of the undissolved material, $V_{net,b}$, was obtained, as described by Equation 20. The volume of the particles, $V_{np,b}$, and the volume of the slug, $V_{nSl,b}$, which remained undissolved at time t_b, were estimated using Equations 21 and 22. The slug radius, $r_{nSl,b}$, after diffusion at time t_b was calculated from Equation 23. This radius value was substituted back into Equation 14, and the iterative process continued until the end of the dissolution test was reached. In this study, the dissolution test was completed after 60 minutes of simulation time.

$$V_{dif,b} = \frac{C(t_b)V_L}{\rho_{Sl}}$$ Equation 19

$$V_{net,b} = V_{Sl0} - V_{dif,b}$$ Equation 20

$$V_{np,b} = V_{net,b}\left(\frac{V_{Lp,b} + V_{p,b}}{V_{Sl,b} + V_{Lp,b} + V_{p,b}}\right)$$ Equation 21

$$V_{nSl,b} = V_{net,b} - V_{np,b}$$ Equation 22

$$r_{nSl,b} = \left(\frac{3V_{nSl,b}}{4\pi}\right)^{\frac{1}{3}}$$ Equation 23

To calculate the surface area of all the disintegrated particles, the size and number of the particles had to be determined. If the size of each disintegrated particle is known, the surface area can be obtained from the surface area equation for a sphere. Furthermore, if the number of particles for each particle size is also known, then the total surface area of all the disintegrated particles can be determined.

Since the slug was only lightly compressed, it could be assumed that the particle size distribution of the disintegrated particles would follow the particle size distribution of the original powder blend at time t_0. This was accomplished by adopting the ascorbic acid particle size distribution data measured by Heda *et al*. [45]. However, as the unbroken slug continues to disintegrate, the disintegrated particles from earlier time intervals may either dissolve via a diffusion process or break into smaller particles. If the slug breaks into smaller particles, the particle size distribution of ascorbic acid at t_0 is no longer pertinent and a new particle size distribution evolves.

To predict the new particle size distribution at each time interval, the Markov chain model was used to provide a discrete solution to the population balance equations of particle breakage [48]. There are many other methods available for conducting population balance modeling. Many of these other methods employ continuous density functions [49-53]. Equation 24 shows a general continuous population balance equation used to model particle breakage processes. Here, f(x,t) is the number density function for size x particles at time t and b(x,y) is the probability distribution for size x particles that are formed from the breakage of size y particles. S(y) and S(x) are the respective breakage frequencies of size y and size x particles [48]. These functions can be used to

build powerful models. However, the complexity of utilizing these functions makes it very difficult to obtain a closed form analytical solution. The Markov chain approach, on the other hand, enables the solution of the population balance equations in a discrete manner. This approach is described by Equation 25 [48]. Here, i is an arbitrary state number representing each discrete particle size with diameter x_i, $N_i(t)$ represents the number of particles in state i at time t, $\Delta N_i(t)$ is the rate of change of the number of particles, b_{ji} is the probability distribution for particles in state i that are formed from the breakage of particles in state j, τ is the time step, and S_i is the breakage frequency of particles in state i.

$$\frac{\partial f(x,t)}{\partial t} = \int_x^\infty b(x,y)S(y)f(y,t)dy - S(x)f(x,t) \qquad \text{Equation 24}$$

$$N_i(t) + \Delta N_i(t) = \sum_{j=i+1}^{n} b_{ji}\tau S_j N_j(t) + (1 - \tau S_i)N_i(t) \qquad \text{Equation 25}$$

The basic underlying principle of the Markov chain model is that the prediction of any future states depends only on the present state and not on any of the past states. This means that as long as the current particle size distribution or the state probability, $a_i(t_b)$, is known, the state probability, $a_i(t_{b+1})$, at a future time, t_{b+1}, can be calculated.

To predict the state probability, $a_i(t_{b+1})$, for particles in state i at time t_{b+1}, the Markovian transition matrix, **P**, needs to be determined. The transition matrix, **P**, as shown in Equation 26, is defined as the sum of a lower triangular matrix, **L**, and a diagonal matrix, **D** [48]. In comparing Equation 25 with Equation 26, **L** and **D** can be determined from Equations 27 and 28, where L_i and B_i are row i of matrix **L** and matrix **B**, respectively, and D_{ii} represents the diagonal value of the matrix **D**.

$$\mathbf{P} = \mathbf{L} + \mathbf{D} \qquad \text{Equation 26}$$

$$L_i = \tau S_i B_i \qquad \text{Equation 27}$$

$$D_{ii} = 1 - \tau S_i \qquad \text{Equation 28}$$

One of the requirements of the Markov chain approach is that two consecutive states should either have a constant interval or a constant ratio; the model may be expressed by uniform discretization or geometric discretization. To discretize the population balance uniformly, the particle size distribution measured by Heda *et al*. [45] was used to estimate the cumulative percentage of seven uniformly spaced particle sizes. The resulting state probability, a_i, for each of the seven state, i, with diameter, x_i, at time $t_b = t_0$ was determined. In addition, the lower limit, d_{i-1}, and upper limit, d_i, of state interval i were calculated from Equations 29 and 30. A detailed description of the computational process of the cumulative particle size distribution and the resulting probability data can be found in Appendix B.

$$d_{i-1} = x_i - \left(\frac{x_{i+1} - x_i}{2} \right) \qquad \text{Equation 29}$$

$$d_i = x_i + \left(\frac{x_{i+1} - x_i}{2} \right) \qquad \text{Equation 30}$$

In this model, where i consists of seven states, the state probability vector, **a**(t), is made up of seven state probabilities, $a_i(t_b)$, while the transition matrix, **P**, is a 7 x 7 matrix with p_{ij} corresponding to the probability of transition from state i to state j. It was assumed that disintegrated particles exist in one of the seven discrete particle size states from state i = 1 to i = 7. In addition, the disintegrated particles that did not dissolve into the dissolution medium via diffusion at earlier time intervals continue to break discretely

according to the particle size distribution, from state i = 7 (largest particle size) to state i = 1 (smallest particle size). The model assumed that no further breakage occurs when a particle size of 74 μm is attained. This implies particles with a diameter of 74 μm will only dissolve into the solution by diffusion. Note that 74 μm was chosen as the particle size where no further breakage occurs because it was the smallest sieve fraction size used by Heda *et al*. [45]. Thus, no data is available for particles below this size range.

To determine the transition matrix, **P**, the breakage frequency, S_i, is defined. In this model, the particles were assumed to break according to the breakage frequency, S_i, described by Equation 31 for all states, i, between 2 and 7, where α is the particle breakage coefficient. At state i = 1, which is the state with the smallest particle size, S_i is equal to zero. This is because it was assumed that no further breakage occurs when 74 μm (state i = 1) is reached. The diagonal matrix, **D**, was estimated by computing D_{ii} using Equation 28, where τ was selected to be 30 seconds under the constraint that τS_i will not be larger than 1.

$$S_i = \alpha x_i^3 \qquad \text{Equation 31}$$

Next, the lower triangular matrix, **L**, was found using Equation 27. Here, B_i is the row i of matrix **B** with component b_{ji}. Assuming the probability for a parent particle to break into smaller particles with any size was the same, b(x,y) can be described by Equation 32 [48]. The equation describing b(x,y) can be integrated to give b_{ji} in a discrete form. Equation 33 was used to determine b_{ji} when $2 \leq j \leq 7$ and $1 \leq i \leq j$. Otherwise, b_{ji} is equal to zero. This is because only larger particles (state j) can break

into smaller fragments (state i). With b_{ji} being defined, the lower triangular matrix, **L**, can be determined. Equation 34 presents **L** for a n x n matrix.

$$b(x,y)=\frac{6x^2}{y^3} \qquad \text{Equation 32}$$

$$b_{ji}=\frac{2}{d_{j-1}^3}\left(d_i^3-d_{i-1}^3\right) \qquad \text{Equation 33}$$

$$\mathbf{L}=\begin{vmatrix} 0 & 0 & \cdot & \cdot & \cdot & 0 & 0 \\ \tau S_2 b_{21} & 0 & \cdot & \cdot & \cdot & 0 & 0 \\ \tau S_3 b_{31} & \tau S_3 b_{32} & \cdot & \cdot & \cdot & 0 & 0 \\ \cdot & \cdot & \cdot & \cdot & \cdot & \cdot & \cdot \\ \cdot & \cdot & \cdot & \cdot & \cdot & \cdot & \cdot \\ \cdot & \cdot & \cdot & \cdot & \cdot & \cdot & \cdot \\ \tau S_n b_{n1} & \tau S_n b_{n2} & \cdot & \cdot & \cdot & \tau S_n b_{n,n-1} & 0 \end{vmatrix}_{n\times n} \qquad \text{Equation 34}$$

By summing matrices **D** and **L**, the transition matrix, **P**, was obtained. The state probability vector, **a**(t), for any future time step can therefore be evaluated from Equation 35.

$$\mathbf{a}(t+\tau)=\mathbf{a}(t)\mathbf{P} \qquad \text{Equation 35}$$

Knowing the probability, $a_i(t_b)$, of having particle size of state x_i at time t_b, the total volume, $V_i(t_b)$, of the disintegrated particles at each particle size of state x_i can be determined from Equation 36. Since the disintegrated particles were assumed to exist in discrete states of known sizes with each state, x_i, as defined in Appendix B, the surface area, A_{si}, and volume, V_{si}, of the individual disintegrated particle at each state can be found. These are described by Equations 37 and 38, respectively. Consequently, the number of particles, $n_i(t_b)$, in each state, x_i, at time t_b can be determined from Equation 39, and the surface area, $A_{Tpi}(t_b)$, of all the disintegrated particles at each state, x_i, can be

found from Equation 40. Finally, the overall surface area, $A(t_b)$, from all the disintegrated particles, as well as the unbroken slug, that are available for the diffusion process at time t_b can be obtained from Equation 41.

$$V_i(t_b) = V_{Lp,b}\, a_i(t_b) + V_{p,b}\, a_i(t_0) \qquad \text{Equation 36}$$

$$A_{si} = 4\pi x_i^2 \qquad \text{Equation 37}$$

$$V_{si} = \frac{4}{3}\pi x_i^3 \qquad \text{Equation 38}$$

$$n_i(t_b) = \frac{V_i(t_b)}{V_{si}} \qquad \text{Equation 39}$$

$$A_{Tpi}(t_b) = n_i(t_b) A_{si} \qquad \text{Equation 40}$$

$$A(t_b) = \sum_{i=1}^{7} A_{Tpi}(t_b) + A_{Sl,b} \qquad \text{Equation 41}$$

Substituting Equation 41 into Equation 13, an analytical expression that describes slug dissolution process, with the disintegration process being captured through the surface area equation, was established. Equation 42 presents this overall expression.

$$C(t) = C_s\left\{1 - \exp\left[-\frac{k}{V_L}\int_0^t \sum_{i=1}^{7} A_{Tpi}(t_b) + A_{Sl,b}\, dt\right]\right\} \qquad \text{Equation 42}$$

Equation 42 can be conveniently converted into an expression that describes the slug dissolution process via erosion only. This is achieved by setting the breakage coefficient, γ, to zero. Similarly, this equation can be used to describe a pure disintegration process without any diffusion by simply setting the mass transfer coefficient, k, to zero.

4.1.2 Capsule Shell and Overall Dissolution Model Development

The dissolution of a capsule shell was assumed to follow an erosion mechanism and diffuse into the dissolution medium. In the literature, the reported time for this process may be as long as 300 seconds [39]. This is a relatively short amount of time in comparison to the overall capsule dissolution process. Due to this short amount of time, it was assumed that A(t) will be similar to the initial surface area, A_G, of the capsule shell. In addition, the mathematical model assumed that capsule shell dissolution and slug dissolution occur in a sequential fashion. Applying the same general form of the mass transfer equation that describes the amount of drug dissolved per unit volume at a certain time t to the gelatin shell dissolution, Equation 43 was obtained. Here, k_G is the mass transfer coefficient for the gelatin shell, G_s is the saturated solubility of gelatin, and G is the solubility of the gelatin shell at time t. Integration of Equation 43 results in the expression for capsule shell dissolution via an erosion process, resulting in the expression described by Equation 44.

$$\frac{dG}{dt} = \frac{k_G A_G}{V_L}\left(G_s - G\right) \qquad \text{Equation 43}$$

$$G(t) = G_s\left[1 - \exp\left(-\frac{k_G A_G t}{V_L}\right)\right] \qquad \text{Equation 44}$$

The overall capsule dissolution model is comprised of both the capsule shell and capsule slug dissolution processes. This is expressed as Equation 45, where C_T (t) is the overall shell plus slug concentration at time t. The first term on the right of Equation 45 describes the gelatin shell dissolution process from time zero to time t_G. The second term describes the slug dissolution process from time t_G to the end of the dissolution test of

time t. The slug dissolution process usually takes about 60 minutes or more. Therefore, the time, t_G, needed for shell dissolution, which is typically less than five minutes (300 seconds), can be neglected. Consequently, Equation 42 alone is sufficient to describe the capsule dissolution process. In summary, a mathematical model comprising both the erosion process of the capsule shell and the two mass transfer processes that a slug undergoes, the disintegration process and the erosion process, was developed.

$$C_T(t) = G_s\left[1-\exp\left(-\frac{k_G A_G}{V_L}\int_0^{t_G} dt\right)\right] + C_s\left\{1-\exp\left[-\frac{k}{V_L}\int_{t_G}^{t}\sum_{i=1}^{7} A_{Tpi}(t_b) + A_{Sl,b}\,dt\right]\right\} \quad \text{Equation 45}$$

4.2 Mass Transfer Coefficient Estimation

To complete the mathematical model, the mass transfer coefficient for the slug was determined. The methods of estimation are described below.

The mass transfer coefficient of the slug was determined from experimental data as well as from theoretical calculations, in a similar manner as conducted by Bai *et al.* [17]. The integrated form of the mass transfer equation, as described by Equation 46, together with experimental dissolution data from the literature, were used to obtain the experimentally determined mass transfer coefficient of the slug, k_{exp}. Equation 46 assumed that the mass transfer coefficient is independent of time [17]. Here, k_{exp} is the mass transfer coefficient, V_L is the dissolution medium volume, C_t is the drug concentration in the medium at time t (which can be obtained from the experimental dissolution data), C_0 is the initial drug concentration in the medium, C_s is the saturated solubility of the drug, C is the drug concentration in the medium, d_{Sl0} is the initial slug

diameter, ρ_{Sl} is the density of the slug, and β is the height-to-diameter ratio of the slug. The derivation of Equation 46 can be found in Appendix C.

$$k_{\exp} = \frac{V_L}{t}\int_{C_0}^{C_t} \frac{\sqrt{\frac{2}{(1+2\beta)\cdot(C_s - C)}}}{\pi\left[d_{Sl0}^3 - \frac{4(C-C_0)V_L}{\pi\beta\rho_{Sl}}\right]^{2/3}} dC \qquad \text{Equation 46}$$

To calculate the mass transfer coefficient, k_{theo}, of the slug theoretically, the mass transfer coefficient equation for a rotating cylinder as shown in Equation 8, together with the CFD-predicted tangential velocities data as presented in Tables 1 and 2 in Section 2.2, were used. Although the slug is also cylindrical in shape, it is positioned down on its surface side instead of the ends. Additionally, the surface area around the surface is much larger than that of the two ends. Therefore, it is reasonable to use only the mass transfer coefficient equation for a rotating cylinder to estimate the slug mass transfer coefficient. In Equation 8, d_T is the diameter of the tablet. This diameter was estimated by taking the average of the sum of the initial diameter, d_{Sl0}, and initial length, L_{Sl0}, of the slug. The rotating Reynolds number, R_Ω, and the Schmidt number, Sc, are defined according to Equations 47 and 48 [17]. The velocity term, u_Ω, in Equation 47 is the velocity at the periphery of the cylinder, which was assumed to be the tangential velocity, v_θ, of the fluid adjacent to the slug.

$$\mathrm{Re}_\Omega = \frac{\left(\frac{d_{Sl0} + L_{Sl0}}{2}\right)u_\Omega \rho}{\mu} \qquad \text{Equation 47}$$

$$Sc = \frac{\mu}{D_{AB}\rho} \qquad \text{Equation 48}$$

If the same size of tablet and capsule are in the same position in the dissolution vessel, the velocities around them should be similar. Additionally, the CFD-predicted velocity vectors around the tablet surface location as shown in Table 3 are similar with or without a tablet in the vessel. It is reasonable to assume that hydrodynamic effects on a tablet would be similar on a capsule. Therefore, the CFD-predicted tangential velocities from the referenced literature were used to calculate the capsule slug mass transfer coefficient. The mass transfer coefficient values calculated experimentally and theoretically were compared and incorporated into the mathematical expression for the capsule dissolution to complete the model.

4.3 Numerical Simulation and Statistical Analysis

The mass transfer process of capsule dissolution, under the effect of the hydrodynamic conditions of the USP Apparatus II, was mathematically modeled by coupling the mass transfer coefficients. The effects of tangential velocity and slug size on the capsule dissolution profiles, as well as three extreme dissolution cases, were evaluated. The model was validated by statistically comparing the generated dissolution profiles against the published dissolution data. The degree of agreement between the model and published data was evaluated by the similarity factor.

The similarity factor is one of the methods recommended by the FDA for comparing similarities or differences between dissolution profiles [1]. This model-independent approach utilizes a pair-wise procedure to compare dissolution profiles based on the values of a difference factor, f_1, which ranges from 0 to 100, and a similarity factor, f_2, which ranges from $-\infty$ to 100 [17, 54]. If two profiles are extremely different,

the f_2 value will approach -∞. If they are deemed to be identical, then f_2 is 100. The difference factor and the similarity factor represent the absolute differences and the squared differences in population averages between cumulative dissolution values of the reference and test assays at all time points, respectively, where only one sample point is allowed to contain more than 85% dissolution of the drug product [55, 56]. While the difference factor measures the percent error between two dissolution profiles, the similarity factor compares the mean differences in dissolution values between the reference and test samples without accounting for differences within each sample type. The difference factor and similarity factor were determined according to Equations 49 and 50, respectively, where n is the number of time points, R_t is the dissolution value of the reference assay at time t, and T_t is the dissolution value of the test assay at the same time, t [1, 17].

$$f_1 = \left\{ \frac{\sum_{t=1}^{n} |R_t - T_t|}{\sum_{t=1}^{n} R_t} \right\} \times 100 \qquad \text{Equation 49}$$

$$f_2 = 50 \log \left\{ \left[1 + \frac{1}{n} \sum_{t=1}^{n} (R_t - T_t)^2 \right]^{-0.5} \times 100 \right\} \qquad \text{Equation 50}$$

According to the FDA, two dissolution profiles are similar if f_1 lies between 0 and 15 and f_2 lies between 50 and 100 [1]. An f_2 value of 50 corresponds to an average difference of 10% between two dissolution profiles at any time point, and this value increases as the average difference is reduced. If the f_1 and f_2 values of the simulated and

the published dissolution profiles meet these criteria, the mathematical model developed in this study, which combines the mass transfer principles as well as the hydrodynamic effects within the USP Apparatus II, would be considered a valid model to describe capsule dissolution testing.

CHAPTER FIVE

RESULTS

A capsule dissolution model has been developed for a slug inside a gelatin capsule shell in a USP Apparatus II. This chapter presents the results of the model simulations. These include the mathematical expressions for capsule shell and slug dissolutions, the estimation of the mass transfer coefficient, and the simulated capsule dissolution profiles.

5.1 Mathematical Model

The mathematical model was developed under the assumption that the capsule shell dissolution and the slug dissolution occur in a sequential fashion. This assumes that ascorbic acid does not diffuse into the dissolution medium until the gelatin capsule shell has completely dissolved. Equation 44 from Section 4.1.2 describes the capsule shell dissolution process. This equation, however, was not incorporated into the dissolution simulation process since the shell dissolution process is relatively short (within five minutes) compared to the one-hour slug dissolution process. In addition, only the drug concentration is typically being monitored over time when conducting the dissolution experiments. The change in concentration of the capsule shell in the dissolution medium is usually neglected.

The slug dissolution model was developed through a combination of the general form of the mass transfer equation, the theoretical mass transfer coefficient with the use of CFD-predicted tangential velocity, the initial particle size distribution of ascorbic acid

from Heda *et al*. [45], and the probability of generating particles of discrete sizes through the application of the Markov chain. The model development process was discussed in Section 4.1.1. All the computed values for the matrices, **D**, **L**, and **P**, of the Markov chain, which are essential for the state probability vector estimation, can be found in Appendix D. These values were calculated with the particle breakage coefficient, α, equal to 10^{-10} $\mu m^{-3}s^{-1}$ and the time step, τ, equal to 30 seconds. A graph showing the state probability vector, **a**(t), for particle size distribution from zero to 60 minutes is also presented in Appendix D. The state probability vector is required in the model simulation to account for particle breakage during dissolution. The result is a mathematical expression that describes the slug dissolution process via pure disintegration, pure erosion, or a combination of both as presented by Equation 42.

5.2 Mass Transfer Coefficients

A mass transfer coefficient was determined experimentally and theoretically. Experimental data obtained from Heda *et al*. [45], as well as the ascorbic acid slug and the dissolution system properties, are reported in Tables 5 and 6, respectively. The dissolution data were plotted and the profile was fitted with a fourth order polynomial equation as shown in Figure 10. The polynomial equation was used to estimate discrete concentration values as a function of time at one-minute intervals up to 40 minutes. The concentration obtained from this polynomial equation started to diverge from the experimental data beyond 40 minutes. The values obtained, together with the properties of ascorbic acid and the dissolution system, were incorporated into Equation 46. The

experimental mass transfer coefficient, obtained by numerical integration of Equation 46 from time zero to 40 minutes, was 106.61 mm/min.

Table 5. Dissolution data of the ascorbic acid slug in size 1 capsules.

T (minutes)	C (%)
3	14
5	27
7	38
10	46
15	59
30	84
45	95
60	100

Table 6. Properties of the ascorbic acid slug and dissolution system used in k_{exp} estimation.

Properties	Values
V_L (mL)	1000
L_{Sl0} (mm)	16.46
d_{Sl0} (mm)	6.3
β	2.61
V_{Sl0} (mm^3)	513.10
ρ_{Sl} (mg/mm^3)	0.49
C_s (mg/mL)	0.25
C_0 (mg/mL)	0

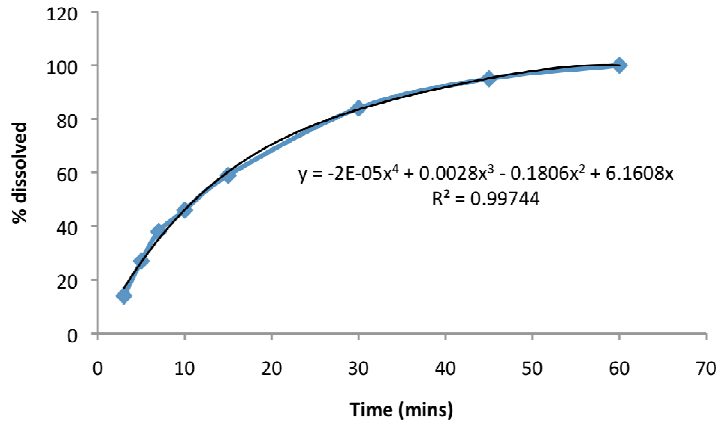

Figure 10. Dissolution graph and polynomial fit of ascorbic acid.

To estimate the theoretical mass transfer coefficient, the tangential velocity of the system was first determined from the CFD-predicted data presented in Tables 1, 2, and 3. With the slug resting on its side during dissolution testing, the height of the slug from the bottom of the vessel was approximately 6.3 mm. Figure 11 figuratively presents the capsule location inside a dissolution vessel. Assuming the slug was located at the center of the vessel and the rotational axis was at the center of the slug, the longer side of the slug would be located at about 8.23 mm from the center of the shaft, which is half of the length of the slug. The shorter side of the slug, on the other hand, would be located at about 3.15 mm from the shaft center. This is approximately half the diameter of the slug. Putting these dimensions together and comparing to Tables 1, 2, and 3, the tangential velocity should be roughly between 0.029 m/s to 0.058 m/s. The mass transfer coefficient was estimated by selecting three tangential velocities from this range: the lower limit, the upper limit, and the average value. Equations 8, 10, 47, and 48 were used to estimate the theoretical mass transfer coefficient, where k_{theo} is equal to k_{side} in

Equation 8. The values of the variables, such as the properties of the dissolution medium and ascorbic acid that were used in determining the mass transfer coefficient with the average tangential velocity, are reported in Appendix E. Although the actual dissolution medium used in the study was 0.1N HCl, properties of water were used in these equations. The tangential velocities and the corresponding theoretical mass transfer coefficients are presented in Table 7. The theoretical mass transfer coefficient estimated from this method was found to range from 0.29 mm/min to 0.47 mm/min, depending on the magnitude of the tangential velocity.

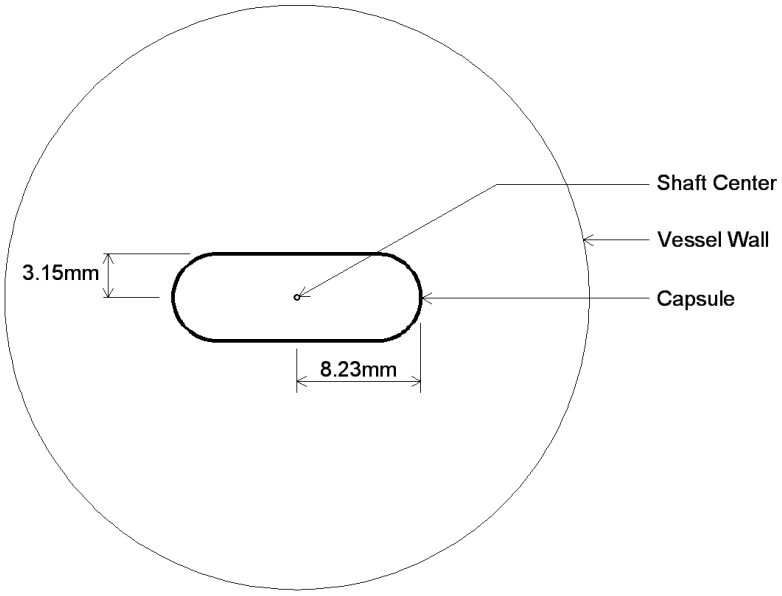

Figure 11. Location of capsule inside dissolution vessel (top view).

Table 7. Tangential velocities and theoretical mass transfer coefficients.

v_θ (m/s)	v_θ (mm/min)	k_{theo} (mm/min)	Notes
0.029	1740	0.29	Lower limit
0.044	2640	0.39	Mid-point average
0.058	3480	0.47	Upper limit

5.3 Simulated Dissolution Profiles and Statistical Comparison

The estimated mass transfer coefficients and the mathematical model were coupled together to simulate dissolution profiles. The effects of tangential velocity, as well as the size of the slug on the dissolution profile, were also evaluated. In addition, three extreme dissolution cases were simulated. Values for the slug breakage coefficient and the particle breakage coefficient were selected such that the simulated profiles could be best fitted with experimental data. Table 8 reports the variables that have constant values for all the model simulations in this study.

Table 8. Variables with constant values in the capsule dissolution model simulation.

Variables	Value	Notes
V_L (mL)	1000	Dissolution medium
C_s (mg/mL)	0.25	Saturated drug solubility
τ (s)	30	Breakage time step

5.3.1 Dissolution Profile with Experimental Mass Transfer Coefficient

First, a dissolution profile was simulated by incorporating the experimental mass transfer coefficient into the model. Table 9 presents the values of the variables used to simulate this dissolution profile. Figure 12 presents the resulting profile with the use of the experimental mass transfer coefficient. The experimental dissolution profile from Heda *et al*. [45] is also included in these figures for comparison purposes. It is very clear that the experimental mass transfer coefficient was over-estimated, resulting in an immediate dissolution profile.

Table 9. Variables used in the capsule dissolution model simulation with k_{exp}.

Variables	Value	Notes
L_{Sl0} (mm)	16.46	Slug length
d_{Sl0} (mm)	6.3	Slug diameter
V_{Sl0} (mm^3)	513.10	Slug volume
r_{Sl0} (mm)	4.97	Slug volume equivalent sphere radius
ρ_{Sl} (mg/mm^3)	0.49	Slug density
v_θ (mm/min)	2640	Tangential velocity
k_{exp} (mm/min)	106.61	Mass transfer coefficient (experimental)
γ (mg/mm^4)	$2*10^{-10}$	Slug breakage coefficient
α ($\mu m^{-3}\ s^{-1}$)	10^{-10}	Particle breakage coefficient

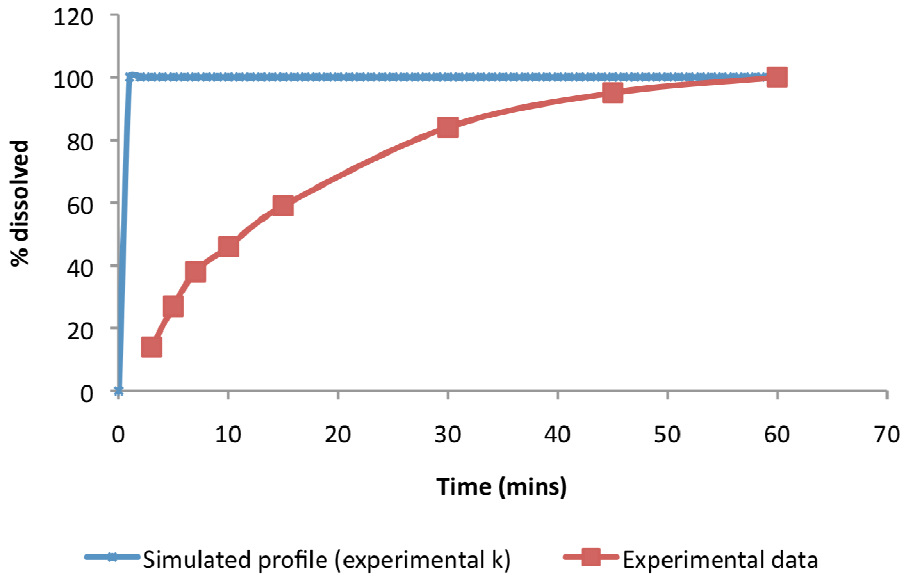

Figure 12. Simulated dissolution profile with experimental mass transfer coefficient (k_{exp} = 106.61 mm/min; $\gamma = 2*10^{-10}$ mg/mm^4; $\alpha = 10^{-10}$ $\mu m^{-3}\ s^{-1}$) and experimental dissolution data.

5.3.2 Dissolution Profiles with Different Tangential Velocities—Theoretical Mass Transfer Coefficients

The three tangential velocities and their corresponding theoretically estimated mass transfer coefficients, presented in Table 7, were incorporated into the capsule

dissolution model. The variables used to simulate these profiles are reported in Table 10. The resulting simulated profiles are presented in Figures 13 to 15. Unlike the profile generated using the experimental mass transfer coefficient, the three dissolution profiles simulated using theoretical mass transfer coefficients gave profiles fairly similar to the experimental data.

Table 10. Variables used in the capsule dissolution model simulation—k_{theo}.

Variables	Lower limit	Mid-point	Upper limit	Notes
L_{Sl0} (mm)	16.46			Slug length
d_{Sl0} (mm)	6.3			Slug diameter
V_{Sl0} (mm^3)	513.10			Slug volume
r_{Sl0} (mm)	4.97			Slug volume equivalent sphere radius
ρ_{Sl} (mg/mm^3)	0.49			Slug density
v_θ (mm/min)	1740	2640	3480	Tangential velocity
k_{theo} (mm/min)	0.29	0.39	0.47	Mass transfer coefficient (theoretical)
γ (mg/mm^4)	$2*10^{-10}$			Slug breakage coefficient
α ($\mu m^{-3}\ s^{-1}$)	10^{-10}			Particle breakage coefficient

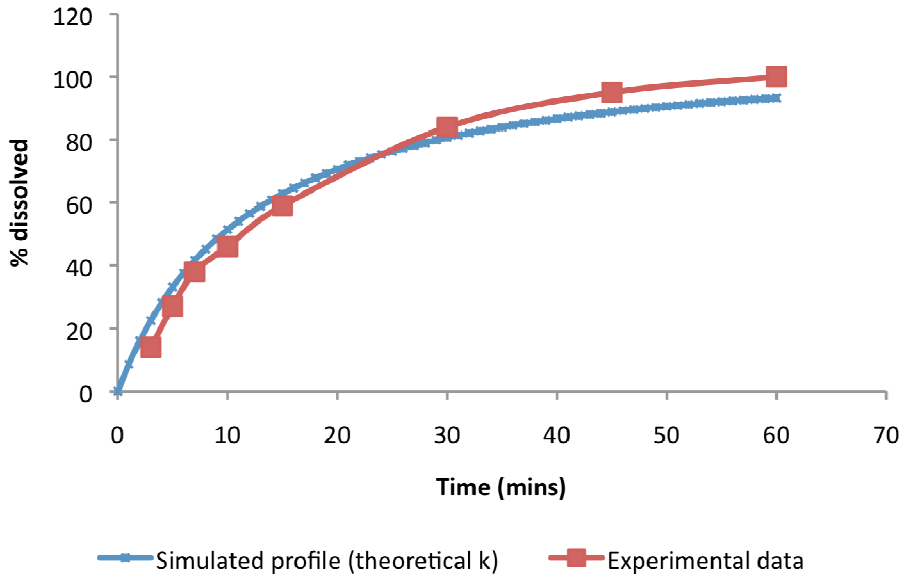

Figure 13. Dissolution profile with the lower limit of tangential velocity (v_θ = 1740 mm/min; k_{theo} = 0.29 mm/min; $\gamma = 2*10^{-10}$ mg/mm^4; $\alpha = 10^{-10}$ μm^{-3} s^{-1}) and experimental dissolution data.

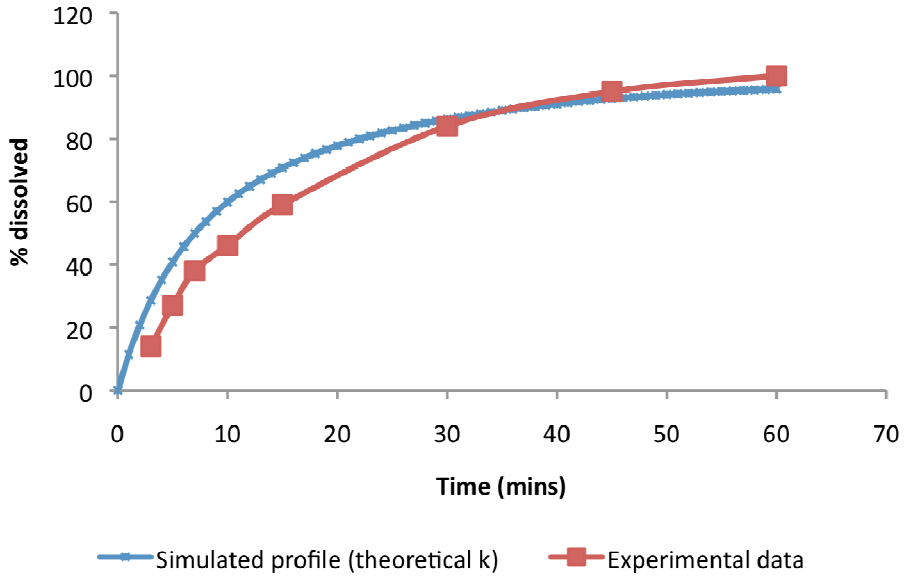

Figure 14. Simulated dissolution profile with average tangential velocity (v_θ = 2640 mm/min; k_{theo} = 0.39 mm/min; $\gamma = 2*10^{-10}$ mg/mm^4; $\alpha = 10^{-10}$ μm^{-3} s^{-1}) and experimental dissolution data.

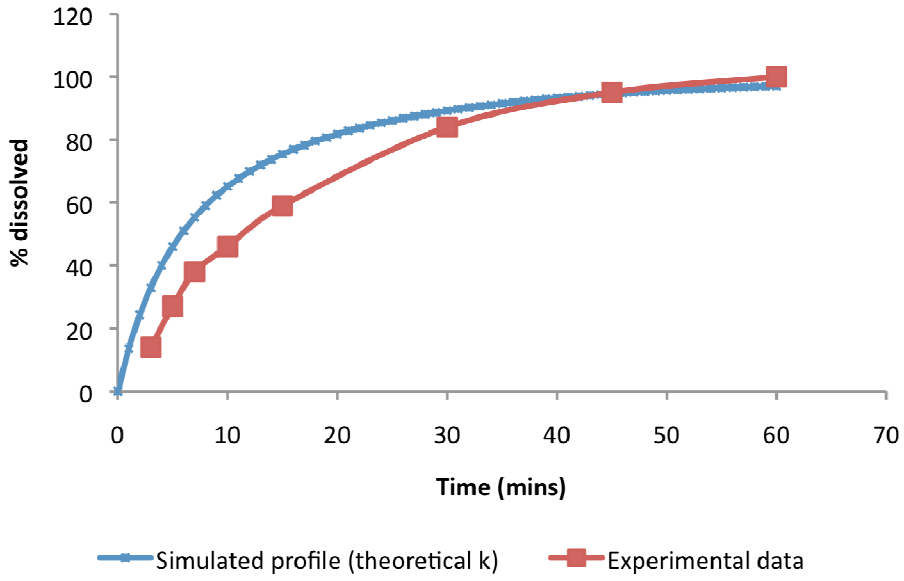

Figure 15. Dissolution profile with the upper limit of tangential velocity (v_θ = 3480 mm/min; k_{theo} = 0.47 mm/min; $\gamma = 2*10^{-10}$ mg/mm^4; $\alpha = 10^{-10}$ μm^{-3} s^{-1}) and experimental dissolution data.

Furthermore, the capsule in this study was assumed to be centrally located in the vessel. To check the validity of this assumption, a tangential velocity that corresponds to an off-centered location in the vessel was incorporated into the model. The location selected was at a radius of approximately 35 mm from the center of the shaft and 19.05 mm from the vessel bottom, as shown in Figure 16. This gives a tangential velocity of 4680 mm/min and a mass transfer coefficient of 0.57 mm/min. The variables incorporated into the model to simulate the dissolution profile for an off-centered capsule are reported in Table 11. The resulting profile is presented in Figure 17.

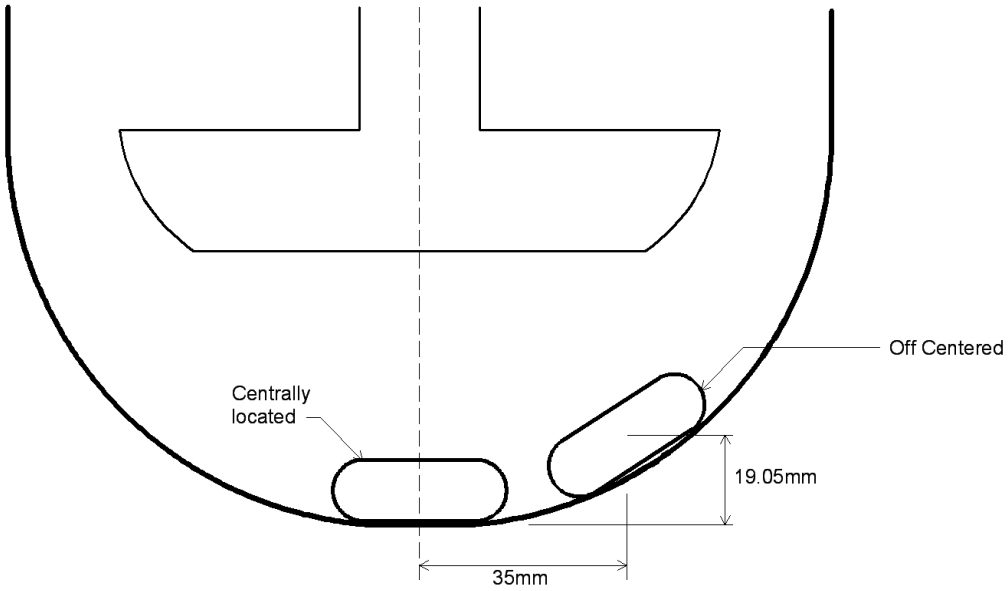

Figure 16. Centrally located and off-centered capsules inside a dissolution vessel.

Table 11. Variables used in the capsule dissolution model simulation—off-centered capsule.

Variables	Value	Notes
L_{Sl0} (mm)	16.46	Slug length
d_{Sl0} (mm)	6.3	Slug diameter
V_{Sl0} (mm^3)	513.10	Slug volume
r_{Sl0} (mm)	4.97	Slug volume equivalent sphere radius
ρ_{Sl} (mg/mm^3)	0.49	Slug density
v_θ (mm/min)	4680	Tangential velocity
k (mm/min)	0.57	Mass transfer coefficient
γ (mg/mm^4)	$2*10^{-10}$	Slug breakage coefficient
α ($\mu m^{-3}\ s^{-1}$)	10^{-10}	Particle breakage coefficient

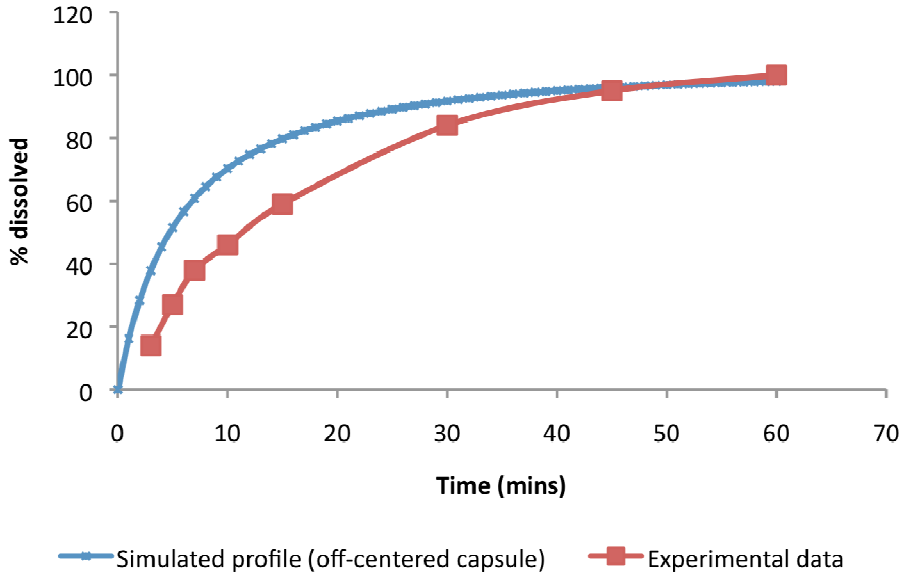

Figure 17. Dissolution profile with tangential velocity corresponds to an off-centered capsule (v_θ = 4680 mm/min; k = 0.57 mm/min; $\gamma = 2*10^{-10}$ mg/mm^4; $\alpha = 10^{-10}$ μm^{-3} s^{-1}) and experimental dissolution data.

5.3.3 Dissolution Profile with Smaller Slug Dimension

The effect of slug dimension was also investigated. Instead of assuming that the capsule body was fully filled with the slug materials, it was assumed that the capsule was only 75% filled. This corresponds to a slug length of 12.35 mm. The overall volume of the slug was therefore reduced by 25%. Since the amount of slug materials remained the same, the density of the slug increased from 0.49 mg/mm^3 to 0.65 mg/mm^3. The variables used to simulate the dissolution profile for a capsule with this reduced filled volume are reported in Table 12. The average tangential velocity of 2640 mm/min was used for this simulation. The resulting simulated profile is presented in Figure 18.

Table 12. Variables used in the capsule dissolution model simulation—smaller slug dimension.

Variables	Value	Notes
L_{Sl0} (mm)	12.35	Slug length
d_{Sl0} (mm)	6.3	Slug diameter
V_{Sl0} (mm^3)	384.82	Slug volume
r_{Sl0} (mm)	4.51	Slug volume equivalent sphere radius
ρ_{Sl} (mg/mm^3)	0.65	Slug density
v_θ (mm/min)	2640	Tangential velocity
k (mm/min)	0.39	Mass transfer coefficient
γ (mg/mm^4)	$2*10^{-10}$	Slug breakage coefficient
α ($\mu m^{-3}\ s^{-1}$)	10^{-10}	Particle breakage coefficient

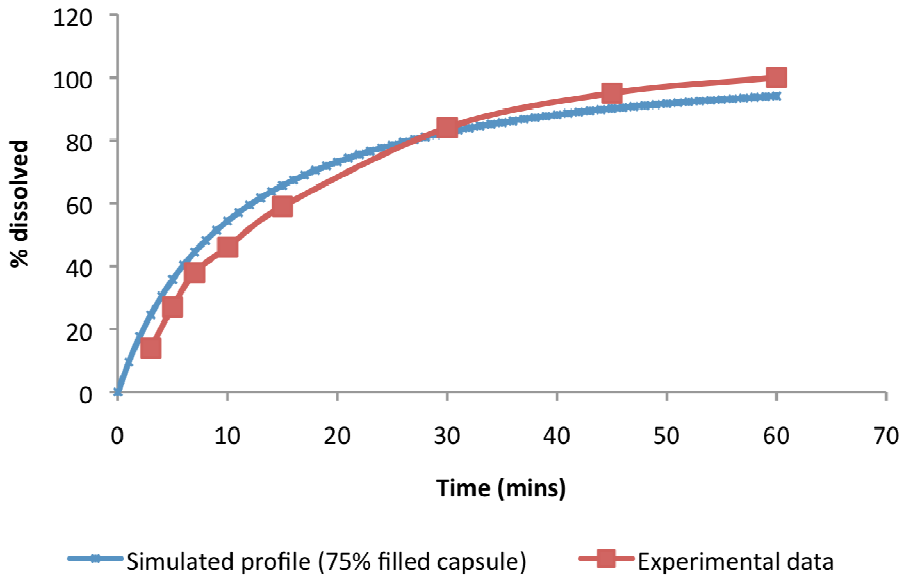

Figure 18. Dissolution profile with a 75% filled capsule (k = 0.39 mm/min; $\gamma = 2*10^{-10}$ mg/mm^4; $\alpha = 10^{-10}$ $\mu m^{-3}\ s^{-1}$) and experimental dissolution data.

5.3.4 Dissolution Profiles for Extreme Cases

To further validate the model, three extreme cases were evaluated. These are the pure erosion process, fast disintegration process, and pure disintegration process without diffusion. For the pure erosion process, the slug breakage coefficient was set as zero.

For the fast disintegration process, the slug breakage coefficient was adjusted such that there was no more unbroken slug one minute after dissolution. V_{Sl} at t equal to one minute should be zero. For the pure disintegration without diffusion process, the mass transfer coefficient was set as zero, and any slug breakage coefficient produced a dissolution profile with the same shape. This is because nothing dissolved and the particles were suspended in the dissolution medium. The variables used to simulate dissolution profiles for these three cases are reported in Table 13. Their dissolution profiles are presented in Figures 19 to 21.

Table 13. Variables used in the capsule dissolution model simulation—extreme cases.

Variables	Pure Erosion	Fast Disintegration	Pure Disintegration	Notes
L_{Sl0} (mm)	16.46			Slug length
d_{Sl0} (mm)	6.3			Slug diameter
V_{Sl0} (mm^3)	513.10			Slug volume
r_{Sl0} (mm)	4.97			Slug volume equivalent sphere radius
ρ_{Sl} (mg/mm^3)	0.49			Slug density
v_θ (mm/min)	2640			Tangential velocity
k (mm/min)	0.39		0	Mass transfer coefficient
γ (mg/mm^4)	0	0.1	$2*10^{-10}$	Slug breakage coefficient
α ($\mu m^{-3}\ s^{-1}$)	0	10^{-10}	10^{-10}	Particle breakage coefficient

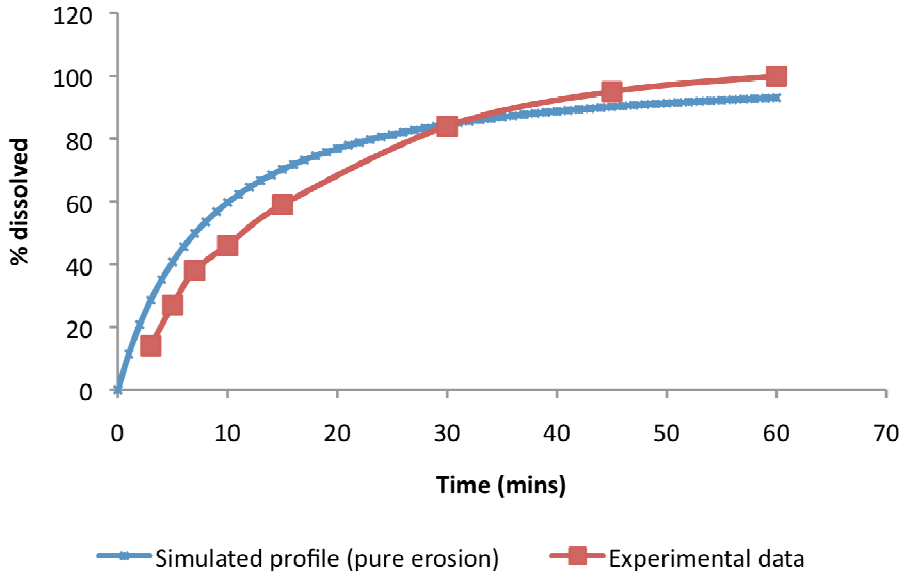

Figure 19. Dissolution profile for pure erosion process (k = 0.39 mm/min; γ = 0 mg/mm^4; α = 0 μm^{-3} s^{-1}) and experimental dissolution data.

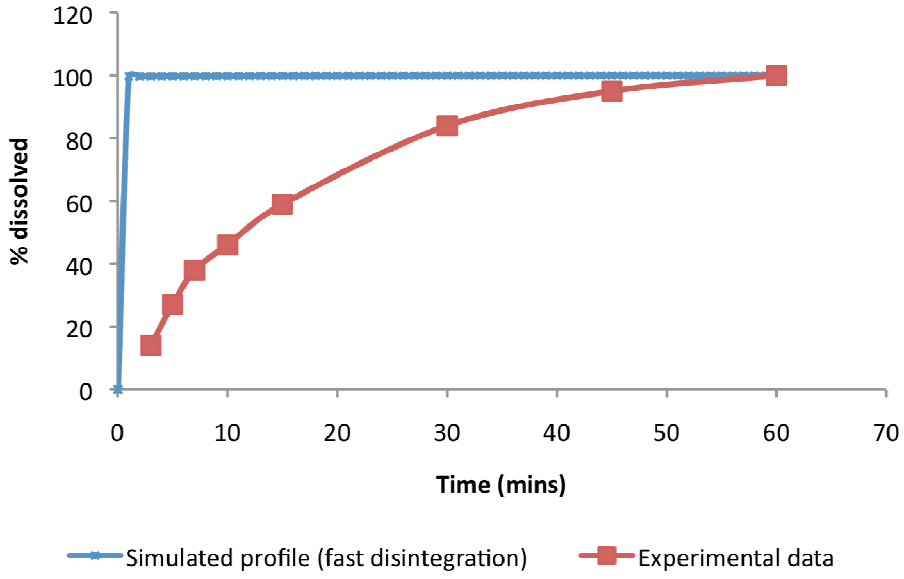

Figure 20. Dissolution profile for fast disintegration process (k = 0.39 mm/min; γ = 0.1 mg/mm^4; α = 10^{-10} μm^{-3} s^{-1}) and experimental dissolution data.

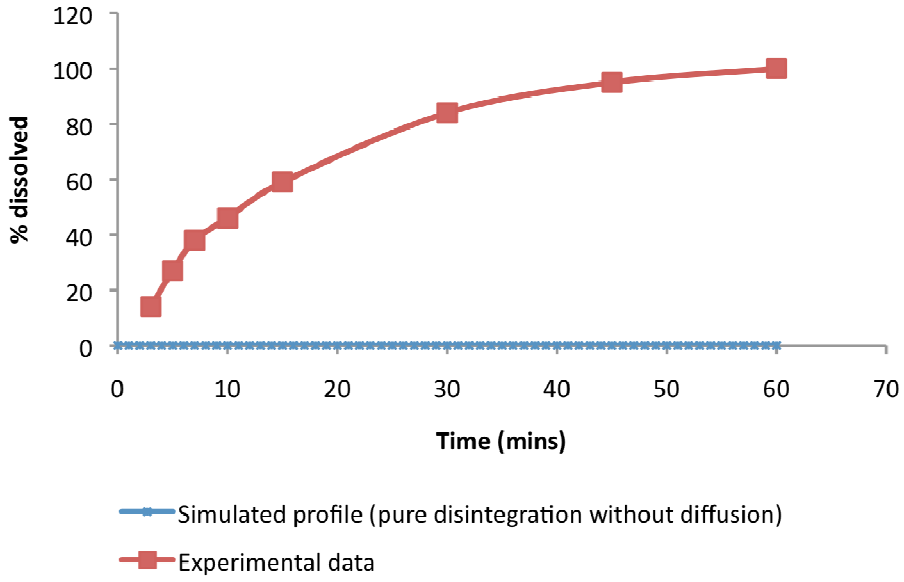

Figure 21. Dissolution profile for pure disintegration process without diffusion (k = 0 mm/min; $\gamma = 2*10^{-10}$ mg/mm^4; $\alpha = 10^{-10}$ μm^{-3} s^{-1}) and experimental dissolution data.

5.3.5 Dissolution Profile with Adjusted Coefficients

The mass transfer coefficient, slug breakage coefficient, and particle breakage coefficient could all be adjusted to bring the simulated dissolution profile closer to the experimental profile. It is expected that a larger mass transfer coefficient would result in a faster dissolution profile, as materials transfer faster from the slug to the dissolution medium. Similarly, a larger slug breakage coefficient and a larger particle breakage coefficient both imply faster material breakage, both of which increase the surface area available for diffusion to take place. According to Equation 3, the rate of drug dissolution is directly proportional to the slug surface area. Therefore, an increase in surface area because of faster material breakage should also result in a faster dissolution profile. By selecting the mass transfer coefficient as 0.23 mm/min, the slug breakage coefficient as $2*10^{-9}$ mg/mm^4, and the particle breakage coefficient as 10^{-10} μm^{-3} s^{-1}, the

simulated and experimental dissolution profiles almost perfectly overlapped with each other. The variables used to simulate this dissolution profile are reported in Table 14. The dissolution profile is presented in Figure 22.

Table 14. Variables used in the capsule dissolution model simulation—adjusted coefficients.

Variables	Value	Notes
L_{Sl0} (mm)	16.46	Slug length
d_{Sl0} (mm)	6.3	Slug diameter
V_{Sl0} (mm^3)	513.10	Slug volume
r_{Sl0} (mm)	4.97	Slug volume equivalent sphere radius
ρ_{Sl} (mg/mm^3)	0.49	Slug density
v_θ (mm/min)	1200	Tangential velocity
k (mm/min)	0.23	Mass transfer coefficient
γ (mg/mm^4)	$2*10^{-9}$	Slug breakage coefficient
α ($\mu m^{-3}\ s^{-1}$)	10^{-10}	Particle breakage coefficient

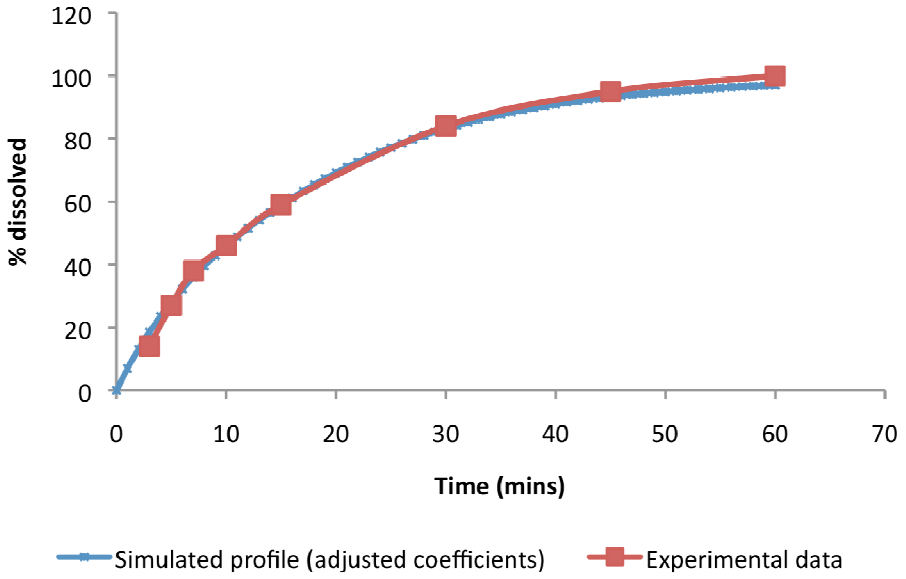

Figure 22. Dissolution profile with coefficients adjusted to match experimental dissolution data (k = 0.23 mm/min; $\gamma = 2*10^{-9}$ mg/mm^4; $\alpha = 10^{-10}$ $\mu m^{-3}\ s^{-1}$).

5.3.6 Statistical Comparison

It is clear that the model with the experimental mass transfer coefficient did not effectively predict the ascorbic acid capsule dissolution profile. However, the simulated dissolution profiles with the theoretically estimated mass transfer coefficients (Figures 13 to 15) are similar to the experimental data. These profiles were statistically compared to the experimental data using the difference factor and similarity factor. The simulated profiles with the off-centered location and the smaller slug dimension, as well as the simulated profile with coefficients adjusted to match the experimental dissolution data, were also statistically compared to the experimental data.

Table 15 lists the dissolution values of the experimental data, R_t, and the simulated profiles, T_t, at time t. These include the dissolution values of the capsules with various tangential velocities, off-centered location, 75% filled volume, and the near-perfect profile with adjusted values. The difference factor, f_1, and the similarity factor, f_2, were reported. For two dissolution profiles to be considered similar, f_1 should be between 0 and 15 while f_2 should be between 50 and 100 [1]. Therefore, the simulated dissolution profile with the lower limit of tangential velocity, and that with the smaller slug dimension (75% filled), are considered to be similar to the experimental data. The difference factor and the similarity factor for the simulated profile, where the coefficients were adjusted to closely match the experimental profile, are 3 and 81, respectively. According to the statistical analysis, the theoretical mass transfer coefficient that best described the experimental dissolution data is 0.29 mm/min.

Table 15. Dissolution values of experimental data and various simulated profiles.

	Experimental data	Lower limit v_θ	Average v_θ	Upper limit v_θ	Off-centered	75% filled	Adjusted values
v_θ (mm/min)	n/a	1740	2640	3480	4680	2640	1200
t (minutes)	R_t (%)	T_t (%)					
3	14	22	29	33	38	24	19
5	27	33	41	46	52	36	28
7	38	42	50	55	61	44	36
10	46	51	60	65	70	54	46
15	59	63	71	75	80	66	59
20	68	71	78	82	85	73	69
30	84	81	86	89	92	83	83
f_1	n/a	10	24	32	42	14	3
f_2	n/a	65	46	39	34	57	81
Similarity	n/a	yes	no	no	no	yes	yes

In summary, mathematical expressions for capsule shell and capsule slug dissolution were developed, the mass transfer coefficient for the dissolution system was determined, and capsule dissolution profiles were simulated. Figure 23 summarizes the key results obtained for each part of the model development process.

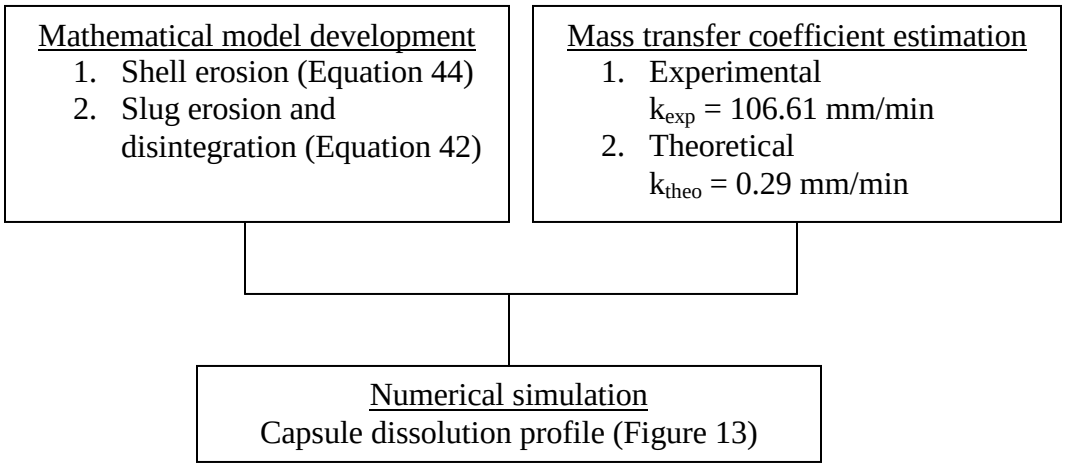

Figure 23. Summary of the key results for capsule dissolution model development.

CHAPTER SIX

DISCUSSION

Mathematical models that describe capsule shell and slug dissolution processes have been generated. In particular, the mathematical model portrays both disintegration and erosion processes for slug dissolution. To validate the model, the mass transfer coefficients were estimated and coupled with the model to simulate several specific cases of the dissolution process. In addition, the simulated profiles were statistically compared with the experimental dissolution data for similarity.

The mass transfer coefficient incorporated in the model was estimated experimentally using experimental dissolution data and theoretically using CFD-predicted tangential velocities. Bai *et al*. [17] found that experimental and theoretical mass transfer coefficients for tablets were on the same order of magnitude where proportionality existed between the two. However, the values obtained from the two methods in this work appeared to be substantially different from each other when capsules were considered. The mass transfer coefficient estimated from experimental dissolution data suggests a rapid mass transfer process, and, subsequently, a fast dissolution profile. Dissolution profiles generated from the model in which the experimental and theoretical mass transfer coefficients were incorporated further revealed the discrepancy of the experimentally estimated value. As shown in Figure 12, the simulated profile using the experimental mass transfer coefficient resulted in an immediate release dissolution profile and did not match the experimental data generated

by Heda *et al*. [45]. The simulated dissolution profile using the theoretical mass transfer coefficient (0.29 mm/min), however, was statistically similar to the experimental profile generated by Heda *et al*. [45]. This could be because the equation used to estimate the mass transfer coefficient from the experimental data assumed a non-disintegrating slug throughout the entire dissolution testing. The tablet that Bai *et al*. [17] studied was a non-disintegrating tablet. Therefore, it is reasonable that their experimental and theoretical mass transfer coefficients agreed with each other.

The tangential velocities obtained from the CFD data to estimate theoretical mass transfer coefficients were chosen under the assumption that the slug was centrally located at the bottom of the vessel during dissolution testing. Three dissolution profiles were simulated using three theoretically estimated mass transfer coefficients. According to the difference and similarity factors, the simulated profile with a theoretical mass transfer coefficient of 0.29 mm/min showed good agreement with the experimental ascorbic acid dissolution curve. This dissolution profile is obtained from the use of the lower limit of tangential velocity with the selected slug breakage coefficient and particle breakage coefficient. The magnitude of the three coefficients together with the good agreement between the two profiles suggest that the ascorbic acid capsule dissolution was dominated by an erosion process with some slug and particle breakages. The other two profiles, simulated using the average and the upper limit of tangential velocities, are not statistically similar to the experimental profile generated by Heda *et al*. [45]. Their difference factors are bigger than 15 and their similarity factors are smaller than 50. The differences in these simulated profiles show that the dissolution profile is very sensitive

to the tangential velocity experienced by the capsule. A capsule can experience different tangential velocity because of a slight change in location. This difference in tangential velocity leads directly to a change in the mass transfer coefficient and therefore a change in the dissolution profile. This is consistent with the observations reported in the literature for tablet dissolutions [9, 10, 15-17, 24, 25, 27].

The effect of tangential velocity on capsule dissolution was also studied using an off-centered capsule. This off-centered position resulted in a higher tangential velocity and therefore a higher theoretical mass transfer coefficient. The resulting simulated profile showed a much faster capsule dissolution rate than the dissolution rates of the centrally located capsule and the capsules studied by Heda *et al*. [45]. Again, this agrees with the results reported in the literature, where a drug product at different locations inside the dissolution vessel experiences different hydrodynamics and therefore dissolution variations [9, 10, 15-19, 21, 24, 25, 27].

There are several factors that could have contributed to the variation observed in the simulated profile using the average tangential velocity in Figure 14. First, the slug was assumed to be the size of a fully filled size 1 capsule. This dimension was not provided by Heda *et al*. [45]. The dimensions of the slug can be important as they determine the density of the slug. An increase in density reduces the dissolution rate. To verify this effect and the importance of the slug dimensions, a simulation was conducted where the capsule was assumed to be 75% filled. This led to a reduction in the length and the volume of the slug. The resulting simulated profile showed that this reduction in filled volume slowed the dissolution rate. Statistical comparison between the simulated

profile and the experimental profile generated by Heda *et al*. [45] shows that they are similar.

In addition to the slug dimensions, the cylindrical slug was modeled as a sphere in the dissolution model development. This could have imposed some differences in the surface area that is available for mass transfer to take place. Furthermore, the mass transfer coefficient was assumed to be independent of time, slug surface area, and particle surface area in this study. According to Equations 3 and 13, surface area changes with time, and a reduction in surface area may change the mass transfer coefficient. Finally, the rate of slug and particles breakage would also potentially change the surface area and hence the dissolution profile.

While the simulated profile with the use of a theoretical mass transfer coefficient of 0.29 mm/min validates the capsule dissolution model, three special cases that were considered to be extreme scenarios were evaluated to confirm the validity of the model. These three cases were the pure erosion process, the fast disintegration process, and the pure disintegration process without diffusion. These cases were selected with the reasoning that if their simulated profiles correctly described the dissolution process, then any dissolution process that is a combination of them could be properly simulated. The simulated profiles of these special cases were found to correctly predict the dissolution trend. The dissolution profile of a pure erosion process should be slower than that of a fast disintegration process. A reduction of mass transfer coefficient to the extreme case of zero collapsed the dissolution profile. Last but not least, an increase in the slug

breakage coefficient, which intuitively increased the surface area, increased the dissolution rate.

The mass transfer coefficient, slug breakage coefficient, and particle breakage coefficient collectively shape the dissolution profile. An increase in the magnitude of any one of them with the rest being held constant, or an increase in the magnitude of all of them, would increase the dissolution rate. Therefore, these three coefficients were adjusted to determine whether a simulated profile that perfectly matched the experimental data could be created. By reducing the value of the mass transfer coefficient and increasing the value of the slug breakage coefficient of the dissolution profile in Figure 13, the simulated profile almost overlapped with the experimental profile. These changes in coefficients correspond to a slower diffusion process yet a slightly faster slug breakage process.

In summary, the mathematical model developed in this study can be regarded as a valid model to describe capsule dissolution testing. It clearly reflects the effect of hydrodynamics on dissolution profile, as reported in the literature [9, 10, 15-19, 21, 24, 25, 27]. It also adequately describes three extreme cases of capsule dissolution processes. In addition, the simulated profile using the theoretical mass transfer coefficient of 0.29 mm/min correlates well with the experimental data. This similarity between the two profiles is validated using statistical analysis.

CHAPTER SEVEN

CONCLUSION AND FUTURE WORK

In conclusion, a mathematical model that combines the mass transfer principles and the hydrodynamic effect within the USP Apparatus II was developed and validated to describe capsule dissolution. The simulated profiles show that the CFD-predicted tangential velocities can be used to estimate the mass transfer coefficient, as suggested in the literature [17]. The simulation results and the estimated mass transfer coefficient show that the dissolution rate changes as a function of capsule location. An off-centered capsule has a much faster dissolution profile than a centrally located capsule. This is consistent with the observations reported in the literature [9, 10, 15-19, 21, 24, 25, 27]. In addition, the model shows that the slug size affects the dissolution profile.

The current model not only simulates the capsule dissolution profile, it also provides insight as to the dissolution mechanism. For example, the model can determine whether a drug product disintegrates or erodes during dissolution testing. The model correctly simulates the trend for three extreme dissolution processes. It can also suggest if the dissolution is dominated by disintegration or erosion process should both processes be present in the system.

Finally, the model shows that the Markov chain can be applied to model particles breakage and their population distribution during the dissolution process. The particle breakage coefficient, the slug breakage coefficient, and the mass transfer coefficient should all be carefully selected to correctly describe capsule dissolution.

In this study, the mass transfer coefficient was assumed to be constant during the dissolution process. To further improve the model, the change in mass transfer coefficient as a function of time, slug surface area, and particle size area should be investigated in future studies.

In addition to the prediction of the experimental dissolution profile, the simulated profiles are shown to correctly predict the dissolution profiles for a pure erosion process, a fast disintegration process, and a pure disintegration process without diffusion. Actual capsule dissolution experiments should be conducted in the future to verify the accuracy of these dissolution profiles.

Lastly, the slug and particle breakage coefficients are not random numbers that can be conveniently modified such that the simulated profile matches the experimental data. These two coefficients, similar to the mass transfer coefficient, technically consist of a group of the slug properties, particle properties, and the dissolution system properties. The slug breakage coefficient should actually consist of the tangential velocity and the density of the slug. Since these two are properties with known values, they were pulled out of the slug breakage coefficient and presented as part of the coefficient of time inside the exponential term in Equation 14. However, there should be many more factors besides these two that determine the slug breakage coefficient. Slug and particle breakage coefficients estimation are definitely worth looking into for future studies.

LIST OF REFERENCES

1. United States Department of Health and Human Services, Food and Drug Administration (1997). *Guidance for industry—Dissolution testing of immediate release solid oral dosage forms* [Online]. Available at http://www.fda.gov/downloads/Drugs/GuidanceComplianceRegulatoryInformation/Guidances/UCM070237.pdf (accessed 11 February 2010). Posted pdf file.

2. United States Pharmacopeia (2010). *Chapter 711* [Online]. Available at http://www.usp.org/pdf/EN/USPNF/chapter711.pdf (accessed 21 February 2010). Posted pdf file.

3. United States Department of Health and Human Services, Food and Drug Administration (2010). *Dissolution methods* [Online]. Available at http://www.accessdata.fda.gov/scripts/cder/dissolution/dsp_SearchResults_Dissolutions.cfm?PrintAll=1 (accessed 13 February 2010). WWW Article.

4. J.L. Cohen, B.B. Hubert, L.J. Leeson, C.T. Rhodes, J.R. Robinson, T.J. Roseman and E. Shefter, "*The development of USP dissolution and drug release standards,*" Pharm. Res., **7**, 983-987 (1990).

5. S.A. Qureshi and J. Shabnam, "*Cause of high variability in drug dissolution testing and its impact on setting tolerances,*" Eur. J. Pharm. Sci., **12**, 271-276 (2001).

6. S.A. Qureshi and I.J. McGilveray, "*Typical variability in drug dissolution testing: study with USP and FDA calibrator tablets and a marketed drug (glibenclamide) product,*" Eur. J. Pharm. Sci., **7**, 249-258 (1999).

7. P. Costa and J.M.S. Lobo, "*Influence of dissolution medium agitation on release profiles of sustained-release tablets,*" Drug Dev. Ind. Pharm., **27**, 811-817 (2001).

8. D.C. Cox, W.B. Furman, L.K. Thornton, T.W. Moore and E.H. Jefferson, "*Systemic error associated with Apparatus 2 of the USP dissolution test III: limitations of calibrators and the USP suitability test,*" J. Pharm. Sci., **72**, 910-913 (1983).

9. J.L. Baxter, J. Kukura and F.J. Muzzio, "*Hydrodynamics-induced variability in the USP apparatus II dissolution test,*" Int. J. Pharm., **292**, 17-28 (2005).

10. United States Department of Health and Human Services, Food and Drug Administration (2005). *Inherent method variability in dissolution testing: The effect of hydrodynamics in the USP II Apparatus* [Online]. Available at http://www.fda.gov/ohrms/dockets/ac/05/briefing/2005-4187B1_01_04-Effect-Hydrodynamics.pdf (accessed 14 January 2010). Posted pdf file.

11. Health Canada (2009). *Drugs recall listing: 2009* [Online]. Available at http://www.hc-sc.gc.ca/dhp-mps/alt_formats/hpfb-dgpsa/pdf/compli-conform/drugs-drogues_recall-retrait_2009-eng.pdf (accessed 22 February 2010). Posted pdf file.

12. Heath Canada (2010). *Drugs recall listing: 2010* [Online]. Available at http://www.hc-sc.gc.ca/dhp-mps/alt_formats/pdf/compli-conform/recall-retrait/_list/drugs-drogues_recall-retrait_2010-eng.pdf (accessed 22 February 2010). Posted pdf file.

13. J.A. Barone, N.G. Lordi, W.G. Byerly and J.L. Colaizzi, "*Comparative dissolution performance of internationally available piroxicam products*," Drug Intelligence and Clinical Pharmacy, **22**, 35-40 (1988).

14. Merck & Co., Inc. (2010). *Bioavailability: Pharmacokinetics: Merck Manual Professional* [Online]. Available at http://www.merckusa.com/mmpe/sec20/ch303/ch303c.html (accessed 24 June 2010). WWW Article.

15. J. Haystead, "*Study highlights flawed dissolution testing procedure*," Pharmaceutical Tech., **27**, 18, 24 (2003).

16. J. Kukura, J.L. Baxter and F.J. Muzzio, "*Shear distribution and variability in the USP Apparatus 2 under turbulent conditions*," Int. J. Pharm., **279**, 9-17 (2004).

17. G. Bai and P.M. Armenante, "*Hydrodynamic, mass transfer, and dissolution effects induced by tablet location during dissolution testing*," J. Pharm. Sci., **98**, 1511-1531 (2009).

18. L.G. McCarthy, G. Bradley, J.C. Sexton, O.I. Corrigan and A.M. Healy, "*Computational fluid dynamics modeling of the paddle dissolution apparatus: Agitation rate, mixing patterns, and fluid velocities*," AAPS PharmSciTech., **5**, Article 31 (2004).

19. J.L. Baxter, J. Kukura and F.J. Muzzio, "*Shear-induced variability in the United States Pharmacopeia Apparatus 2: Modifications to the existing system*," The AAPS Journal, **7**, Article 83 (2006).

20. D.M. D'Arcy, O.I. Corrigan and A.M. Healy, "*Evaluation of hydrodynamics in the basket dissolution apparatus using computational fluid dynamics—dissolution rate implications,*" Eur. J. Pharm. Sci., **27**, 259-267 (2006).

21. G. Bai and P.M. Armenante, "*Velocity distribution and shear rate variability resulting from changes in the impeller location in the USP Dissolution Testing Apparatus II,*" Pharm. Res., **25**, 320-336 (2008).

22. D.M. D'Arcy, A.M. Healy and O.I. Corrigan, "*Towards determining appropriate hydrodynamic conditions for in vitro in vivo correlations using computational fluid dynamics,*" Eur. J. Pharm. Sci., **37**, 291-299 (2009).

23. J. Kukura, P.E. Arratia, E.S. Szalai and F.J. Muzzio, "*Engineering tools for understanding the hydrodynamics of dissolution tests,*" Drug Dev. Ind. Pharm., **29**, 231-239 (2003).

24. G. Bai, P.M. Armenante, R.V. Plank, M. Gentzler, K. Ford and P. Harmon, "*Hydrodynamic investigation of USP dissolution test Apparatus II,*" J. Pharm. Sci., **96**, 2327-2349 (2007).

25. L.G. McCarthy, C. Kosiol, A.M. Healy, G. Bradley, J.C. Sexton and O.I. Corrigan, "*Simulating the hydrodynamic conditions in the United States Pharmacopeia paddle dissolution apparatus,*" AAPS PharmSciTech., **4**, Article 22 (2003).

26. A.M. Healy, L.G. McCarthy, K.M. Gallagher and O.I. Corrigan, "*Sensitivity of dissolution rate to location in the paddle dissolution apparatus,*" J. Pharm. Pharmacol., **54**, 441-444 (2002).

27. D.M. D'Arcy, O.I. Corrigan and A.M. Healy, "*Hydrodynamic simulation (computational fluid dynamics) of asymmetrically positioned tablets in the paddle dissolution apparatus: impact on dissolution rate and variability,*" J. Pharm. Pharmacol., **57**, 1243-1250 (2005).

28. A.A. Noyes and W.R. Whitney, "*The rate of solution of solid substances in their own solutions,*" J. Am. Chem. Soc., **19**, 930-934 (1897).

29. A. Dokoumetzidis and P. Macheras, "*A century of dissolution research: From Noyes and Whitney to the Biopharmaceutics Classification System,*" Int. J. Pharm., **321**, 1-11 (2006).

30. V. Gray, G. Kelly, M. Xia, C. Butler, S. Thomas and S. Mayock, "*The science of USP 1 and 2 dissolution: Present challenges and future relevance,*" Pharm. Res., **26**, 1289-1302 (2009).

31. J. Kukura, P.C. Arratia, E.S. Szalai, K.J. Bittorf and F.J. Muzzio, "*Understanding pharmaceutical flows,*" Pharmaceutical Tech., **26**, 48-72 (2002).

32. M. Crane, N.J. Hurley, L. Crane, A.M. Healy, O.I. Corrigan, K.M. Gallagher and L.G. McCarthy, "*Simulation of the USP drug delivery problem using CFD: experimental, numerical and mathematical aspects,*" Simu. Model. Practice Theo., **12**, 147-158 (2004).

33. R.B. Bird, W.E. Stewart and E.N. Lightfoot, "*The equations of change for isothermal systems,*" in Transport Phenomena, 2nd ed. (John Wiley & Sons, Inc., New York, United States of America, 2007), pp. 77-84.

34. E.L. Paul, V.A. Atiemo-Obeng and S.M. Kresta, Handbook of Industrial Mixing, (John Wiley & Sons, Inc., New Jersey, United States of America, 2004), pp. 259-261.

35. O. Akiti, *Hydrodynamics of a USP dissolution apparatus (August 2005).*

36. R.B. Bird, W.E. Stewart and E.N. Lightfoot, "*Interphase transport in nonisothermal mixtures,*" in Transport Phenomena, 2nd ed. (John Wiley & Sons, Inc., New York, United States of America, 2007), pp. 679.

37. L. Labraga and T. Berkah, "*Mass transfer from a rotating cylinder with and without crossflow,*" Int. J. Heat Mass Transf., **47**, 2493-2499 (2004).

38. C.D. Melia and S.S. Davis, "*Review article: mechanisms of drug release from tablets and capsules. I: disintegration,*" Aliment. Pharmacol. Therap., **3**, 223-232 (1989).

39. I. Chiwele, B.E. Jones and F. Podczeck, "*The shell dissolution of various empty hard capsules,*" Chem. Pharm. Bull., **48**, 951-956 (2000).

40. F. Podczeck and B.E. Jones, "*The in vitro dissolution of theophylline from different types of hard shell capsules,*" Drug Dev. Ind. Pharm., **28**, 1163-1169 (2002).

41. Y. El-Malah and S. Nazzal, "*Hard gelatin and hypromellose (HPMC) capsules: estimation of rupture time by real-time dissolution spectroscopy,*" Drug Dev. Ind. Pharm., **33**, 27-34 (2007).

42. Pfizer, Inc. (2010). *Capsugel products Coni-Snap® Capsules* [Online]. Available at http://www.capsugel.com/products/conisnap_chart.php (accessed 14 June 2010). WWW Article.

43. C.D. Melia and S.S. Davis, "*Review article: mechanisms of drug release from tablets and capsules. 2. dissolution,*" Aliment. Pharmacol. Therap., **3**, 513-525 (1989).

44. A. El-Yazigi, "*Disintegration-dissolution analysis of percent dissolved-time data,*" J. Pharm. Sci., **70**, 535-537 (1981).

45. P.K. Heda, K. Muteba and L.L. Augsburger, "*Comparison of the formulation requirements of dosator and dosing disc automatic capsule filling machines,*" AAPS PharmSci., **4**, Article 17 (2002).

46. R.B. Bird, W.E. Stewart and E.N. Lightfoot, "*Diffusivity and the mechanisms of mass transport,*" in Transport Phenomena, 2nd ed. (John Wiley & Sons, Inc., New York, United States of America, 2007), pp. 530.

47. B.P. Hills and M. Harrison, "*Two-film theory of flavour release from solids,*" Intl. J. Food Sci. Technol., **30**, 425-436 (1995).

48. M. Catak, N. Bas, K. Cronin, J.J. Fitzpatrick and E.P. Byrne, "*Discrete solution of the breakage equation using Markov chains,*" Ind. Eng. Chem. Res., **49**, 8248-8257 (2010).

49. F.C.T. Voon, P.W. Lucas, K.L. Chew and D.A. Luke, "*A simulation approach to understanding the masticatory process,*" J. Theor. Biol., **119**, 251-262 (1986).

50. P.J. Hill and K.M. Ng, "*New discretization procedure for the breakage equation,*" AIChE Journal, **41**, 1204-1216 (1995).

51. P.J. Hill and K.M. Ng, "*Statistics of multiple particle breakage,*" AIChE Journal, **42**, 1600-1611 (1996).

52. M. Harrison, S. Campbell and B.P. Hills, "*Computer simulation of flavor release from solid foods in the mouth,*" J. Agric. Food Chem., **46**, 2736-2743 (1998).

53. B.V. Balakin, A.C. Hoffmann and P. Kosinski, "*Population balance model for nucleation, growth, aggregation, and breakage of hydrate particles in turbulent flow,*" AIChE Journal, **56**, 2052-2062 (2010).

54. P. Costa and J.M.S. Lobo, "*Modeling and comparison of dissolution profiles,*" Eur. J. Pharm. Sci., **13**, 123-133 (2001).

55. V.P. Shah, Y. Tsong, P. Sathe and J.P. Liu, "*In vitro dissolution profile comparison—statistics and analysis of the similarity factor, f_2,*" Pharm. Res., **15**, 889-896 (1998).

56. M.C. Ma, R.P. Lin and J.P. Liu, "*Statistical evaluations of dissolution similarity*," Statistica Sinica, **9**, 1011-1027 (1999).

APPENDIX A

ESTIMATION OF TANGENTIAL VELOCITY

Tangential velocity estimation from Bai *et al*. [24]

The y-axis of the tangential velocity profiles presented by Bai *et al*. [24] represents the tangential velocity normalized to the impeller tip speed, and the x-axis is the radial distance presented as 2r/T, where r is the radial distance from the center of the shaft and T is the vessel diameter with a length of 100.16 mm. Given the values for 2r/T from the x-axis of the graphs presented by Bai *et al*. [24], the radial distance from the center of the shaft can be determined. Table A-1 presents the computed results for r when 2r/T is equal to 0.1 and 0.2.

Table A-1. Determination of the radial distance from the center of the shaft.

2r/T	r (mm)
0.1	5.008
0.2	10.016

Similarly, tangential velocities, v_θ, can be estimated from the y-axis of the graph presented by Bai *et al*. [24]. Given the values for v_θ / v_{tip} from the y-axis, where v_{tip} is the impeller tip speed (0.194 m/s), v_θ can be determined. Tangential velocities at three different locations of iso-surface planes (z = -31.75 mm, z = -37.75 mm, and z = -43.75 mm), where z = 0 represents the intersection between the cylindrical and hemispherical sections of the vessel located 50.8 mm from the bottom of the vessel, were estimated and presented in Table A-2. In addition, the corresponding distance from the bottom of the

vessel for the three locations were calculated by subtracting the absolute value of the vertical location of the iso-surface, z, from 50.8 mm. These are presented in Table A-2.

Table A-2. Tangential velocities at various locations of the vessel.

z (mm)	Distance from vessel bottom (mm)		r (mm)	
			5.008	10.016
-31.75	19.05	v_θ / v_{tip}	0.15	0.3
		v_θ (m/s)	0.029	0.058
-37.75	13.05	v_θ / v_{tip}	0.16	0.3
		v_θ (m/s)	0.031	0.058
-43.75	7.05	v_θ / v_{tip}	0.15	0.29
		v_θ (m/s)	0.029	0.056

Tangential velocity estimation from McCarthy *et al*. [25]

McCarthy *et al*. [25] graphically presented the CFD-predicted tangential velocities for four radial positions on an iso-surface plane 5.3 mm from the bottom of the vessel. These four radial positions are named R = 0.094, R = 0.177, R = 0.262, and R = 0.344, where R is the ratio of the actual radius, r, to the radius of the cylindrical part of the vessel (r_w = 50.8 mm). Therefore, a value of R = 0.094 corresponds to an actual radius, r, of 0.094 * 50.8 mm = 4.7752 mm.

The tangential velocities at each of these four radial positions can be determined from the graph presented by McCarthy *et al*. [25]. The ratio of tangential velocity to paddle tip speed was approximated from the y-axis of the graph for each radial position. The tangential velocity can therefore be estimated by multiplying that ratio by the tip speed (0.196 m/s). For example, the average ratio of tangential velocity to paddle tip speed at R = 0.094 was about 0.15. Therefore, tangential velocity at r = 4.78 mm is estimated to be 0.15 * 0.196 m/s = 0.0294 m/s. Table A-3 presents the actual radial

positions, r, as well as their tangential velocities corresponding to the four normalized radial positions, R.

Table A-3. Tangential velocities at various radial positions in the vessel.

R	r (mm)	v_θ / v_{tip}	v_θ (m/s)
0.094	4.78	0.15	0.029
0.177	8.99	0.25	0.049
0.262	13.31	0.35	0.069
0.344	17.48	0.45	0.088

APPENDIX B

CUMULATIVE PARTICLE SIZE DISTRIBUTION DETERMINATION

Table B-1 and Figure B-1 present the cumulative percentage of ascorbic acid particle size distribution measured by Heda *et al*. [45]. Using the equation of the trend line from Figure B-1, the cumulative percentage of ascorbic acid particle size distribution at various sizes could be determined. The result of seven discrete particle sizes is presented in Table B-2. In addition, the cumulative percentage was normalized to 100%, and the net percentage of each size was also estimated.

Table B-1. Cumulative percentage of ascorbic acid particle size distribution.

Size (μm)	Cumulative percentage
74	100
88	98
125	93
177	85
250	70
590	8

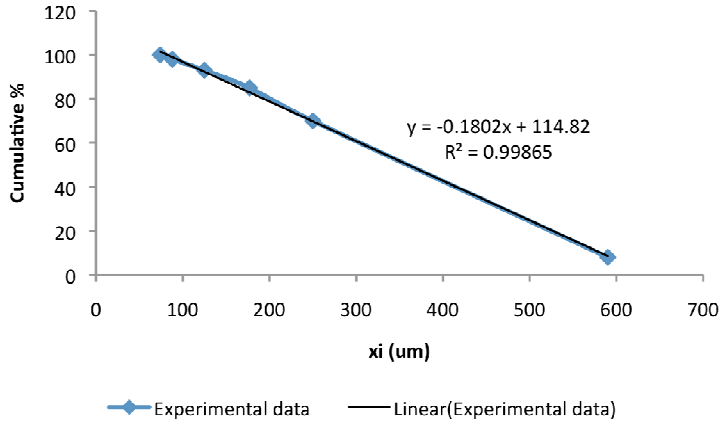

Figure B-1. Cumulative percent lots of ascorbic acid particle size distribution.

Table B-2. Cumulative and net percentage of ascorbic acid particle size distribution.

Size (μm)	Cumulative percentage (predicted)	Cumulative percentage (normalized)	Net percentage
74	101	100	15
160	86	85	16
246	70	69	15
332	55	54	15
418	39	39	15
504	24	24	16
590	9	8	8

Table B-3 presents the resulting state probability, a_i, for each of the seven state, i, with diameter x_i at time $t_b = t_0$ as well as the lower limit, d_{i-1}, and upper limit, d_i, of state interval i.

Table B-3. The state probability for particles with diameter, x_i, at time t_0 and the limit of state interval i.

i	x_i (μm)	a_i	d_{i-1}	d_i
1	74	0.15	31	117
2	160	0.16	117	203
3	246	0.15	203	289
4	332	0.15	289	375
5	418	0.15	375	461
6	504	0.16	461	547
7	590	0.08	547	633

APPENDIX C

DERIVATION OF EXPERIMENTAL MASS TRANSFER COEFFICIENT

A cylindrical slug is defined to have initial diameter, d_{Sl0}, and initial length, L_{Sl0}. Assume the slug erodes throughout the dissolution test such that the ratio of length to diameter remains constant during dissolution testing, β can be defined as Equation C-1. The surface area, A_{Sl}, and the volume, V_{Sl}, of the cylindrical slug can therefore be expressed as Equations C-2 and C-3, respectively.

$$\beta = \frac{L_{Sl}}{d_{Sl}} \qquad \text{Equation C-1}$$

$$A_{Sl} = \pi d_{Sl}^2 \left(\frac{1+2\beta}{2} \right) \qquad \text{Equation C-2}$$

$$V_{Sl} = \frac{\beta \pi d_{Sl}^3}{4} \qquad \text{Equation C-3}$$

From mass balance, a decrease in mass from the solid slug should result in an increase in drug concentration in the medium. This is presented by Equation C-4.

$$\frac{\rho_{Sl}\left(V_{Sl0} - V_{Sl}\right)}{V_L} = C - C_0 \qquad \text{Equation C-4}$$

Assume the density of the slug is constant and substitute Equation C-3 into Equation C-4, an expression for the slug diameter, d_{Sl}, can be obtained, as shown in Equation C-5. Equation C-2 and Equation C-5 together give Equation C-6. Incorporate Equation C-6 into Equation 3 and integrate the equation gives Equation 46. The experimental mass transfer coefficient is obtained by integrating Equation 46 from zero to 40 minutes using Excel™.

$$d_{Sl} = \left(d_{Sl0}^3 - \frac{4(C - C_0)V_L}{\beta \pi \rho_{Sl}} \right)^{\frac{1}{3}}$$ Equation C-5

$$A(C) = \pi \left(d_{Sl0}^3 - \frac{4(C - C_0)V_L}{\beta \pi \rho_{Sl}} \right)^{\frac{2}{3}} \left(\frac{1 + 2\beta}{2} \right)$$ Equation C-6

APPENDIX D

MARKOV CHAIN

With α having a value of 10^{-10} $\mu m^{-3}s^{-1}$ and τ equals to 30 seconds, the calculated values for the matrices, **D**, **L**, and **P**, are presented by Equations D-1, D-2, and D-3, respectively. The state probability vector, **a**(t), was estimated and the graph showing **a**(t) for particle size distribution from zero to 60 minutes is presented in Figure D-1.

$$\mathbf{D} = \begin{vmatrix} 1 & 0 & 0 & 0 & 0 & 0 & 0 \\ 0 & 0.988 & 0 & 0 & 0 & 0 & 0 \\ 0 & 0 & 0.955 & 0 & 0 & 0 & 0 \\ 0 & 0 & 0 & 0.890 & 0 & 0 & 0 \\ 0 & 0 & 0 & 0 & 0.781 & 0 & 0 \\ 0 & 0 & 0 & 0 & 0 & 0.616 & 0 \\ 0 & 0 & 0 & 0 & 0 & 0 & 0.384 \end{vmatrix} \quad \text{Equation D-1}$$

$$\mathbf{L} = \begin{vmatrix} 0 & 0 & 0 & 0 & 0 & 0 & 0 \\ 0.024 & 0 & 0 & 0 & 0 & 0 & 0 \\ 0.017 & 0.072 & 0 & 0 & 0 & 0 & 0 \\ 0.014 & 0.062 & 0.143 & 0 & 0 & 0 & 0 \\ 0.013 & 0.056 & 0.131 & 0.238 & 0 & 0 & 0 \\ 0.012 & 0.053 & 0.124 & 0.224 & 0.355 & 0 & 0 \\ 0.012 & 0.051 & 0.119 & 0.215 & 0.341 & 0.495 & 0 \end{vmatrix} \quad \text{Equation D-2}$$

$$\mathbf{P} = \begin{vmatrix} 1 & 0 & 0 & 0 & 0 & 0 & 0 \\ 0.024 & 0.988 & 0 & 0 & 0 & 0 & 0 \\ 0.017 & 0.072 & 0.955 & 0 & 0 & 0 & 0 \\ 0.014 & 0.062 & 0.143 & 0.890 & 0 & 0 & 0 \\ 0.013 & 0.056 & 0.131 & 0.238 & 0.781 & 0 & 0 \\ 0.012 & 0.053 & 0.124 & 0.224 & 0.355 & 0.616 & 0 \\ 0.012 & 0.051 & 0.119 & 0.215 & 0.341 & 0.495 & 0.384 \end{vmatrix} \quad \text{Equation D-3}$$

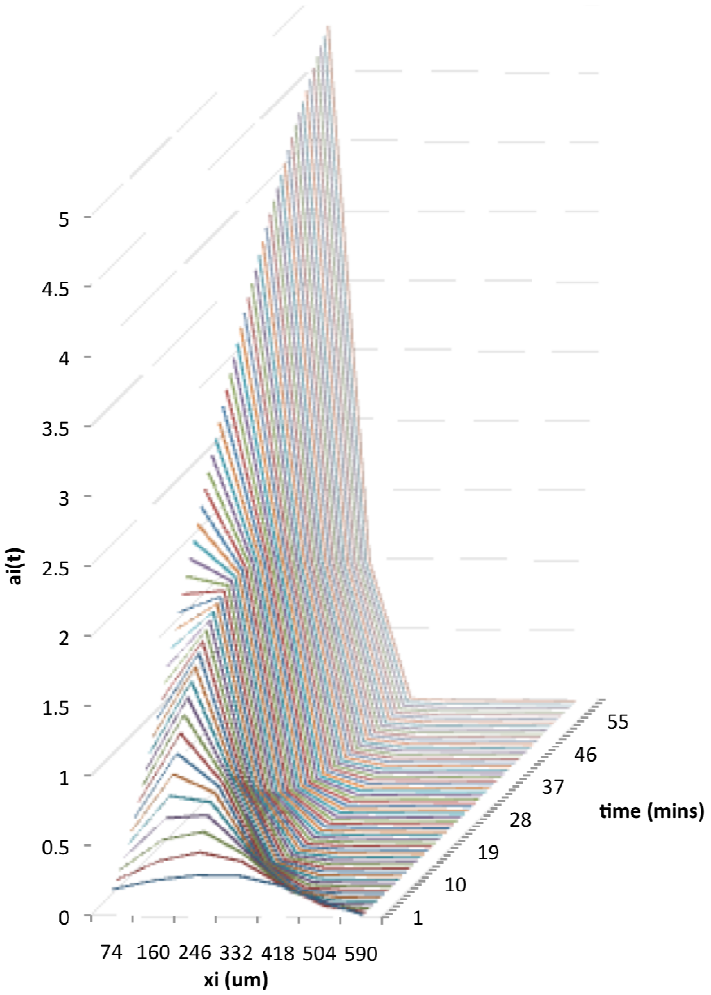

Figure D-1. Particle size distribution from zero to 60 minutes.

APPENDIX E

VARIABLES FOR MASS TRANSFER COEFFICIENT ESTIMATION

Table E-1 reports the values of the properties of the dissolution medium and ascorbic acid used in determining the theoretical mass transfer coefficient.

Table E-1. Properties of dissolution medium and ascorbic acid used in k_{theo} estimation where v_θ = 2640 mm/min.

Properties	Values	Notes
d_{Sl0} (mm)	6.3	Slug diameter
L_{Sl0} (mm)	16.46	Slug length
v_θ (mm/min)	2640	n/a
ρ (g/mm^3)	0.001	Water
μ (g/mm min)	0.042	Water
Re	715	Dissolution system
ψ_B	2.6	Water
M (g/mol)	18.02	Water
T_K (K)	310	Water
M_{AC} (g/mol)	176.13	Ascorbic acid
ρ_{AC} (g/cm^3)	1.65	Ascorbic acid
V_A (cm^3/mol)	106.7	Ascorbic acid
D_{AB} (mm^2/min)	0.0572	Ascorbic acid/water
Sc	735	Dissolution system